

# Re-evaluating $^{142}\text{Nd}/^{144}\text{Nd}$ in lunar mare basalts with implications for the early evolution and bulk Sm/Nd of the Moon

Alan D. Brandon<sup>a,\*</sup>, Thomas J. Lapen<sup>b</sup>, Vinciane Debaille<sup>c</sup>, Brian L. Beard<sup>d</sup>,  
Kai Rankenburg<sup>e</sup>, Clive Neal<sup>f</sup>

<sup>a</sup> NASA Johnson Space Center, Mail Code KR, 2101 Nasa Parkway, Houston, TX 77058, USA

<sup>b</sup> Earth and Atmospheric Sciences, University of Houston, 4800 Calhoun Rd. Houston, TX 77204-5007, USA

<sup>c</sup> Département des Sciences de la terre et de l'Environnement, Université Libre de Bruxelles, CP160/02, 50, Av. F.D. Roosevelt, 1050 Brussels, Belgium

<sup>d</sup> Department of Geology and Geophysics, University of Wisconsin-Madison, 1215 W. Dayton Street, Madison, WI 53706, USA

<sup>e</sup> Freie Universität Berlin, Institut für Geologische Wissenschaften, Fachrichtung Geochemie, Malteserstr. 74-100, Haus B, 12249 Berlin, Germany

<sup>f</sup> Department of Civil Engineering and Geological Sciences, University of Notre Dame, Notre Dame, IN 48556, USA

Received 31 March 2009; accepted in revised form 9 July 2009; available online 16 July 2009

## Abstract

The Moon likely accreted from melt and vapor ejected during a cataclysmic collision between Proto-Earth and a Mars-sized impactor very early in solar system history. The identical W, O, K, and Cr isotope compositions between materials from the Earth and Moon require that the material from the two bodies were well-homogenized during the collision process. As such, the ancient isotopic signatures preserved in lunar samples provide constraints on the bulk composition of the Earth. Two recent studies to obtain high-precision  $^{142}\text{Nd}/^{144}\text{Nd}$  ratios of lunar mare basalts yielded contrasting results. In one study, after correction of neutron fluence effects imparted to the Nd isotope compositions of the samples, the coupled  $^{142}\text{Nd}$ – $^{143}\text{Nd}$  systematics were interpreted to be consistent with a bulk Moon having a chondritic Sm/Nd ratio [Rankenburg K., Brandon A. D. and Neal C. R. (2006) Neodymium isotope evidence for a chondritic composition of the Moon. *Science* **312**, 1369–1372]. The other study found that their data on the same and similar lunar mare basalts were consistent with a bulk Moon having a superchondritic Sm/Nd ratio [Boyet M. and Carlson R. W. (2007) A highly depleted Moon or a non-magma origin for the lunar crust? *Earth Planet. Sci. Lett.* **262**, 505–516]. Delineating between these two potential scenarios has key ramifications for a comprehensive understanding of the formation and early evolution of the Moon and for constraining the types of materials available for accretion into large terrestrial planets such as Earth.

To further examine this issue, the same six lunar mare basalt samples measured in Rankenburg et al. [Rankenburg K., Brandon A. D. and Neal C. R. (2006) Neodymium isotope evidence for a chondritic composition of the Moon. *Science* **312**, 1369–1372] were re-measured for high-precision Nd isotopes using a multidynamic routine with reproducible internal and external precisions to better than  $\pm 3$  ppm ( $2\sigma$ ) for  $^{142}\text{Nd}/^{144}\text{Nd}$  ratios. The measurements were repeated in a distinct second analytical campaign to further test their reproducibility. Evaluation of accuracy and neutron fluence corrections indicates that the multidynamic Nd isotope measurements in this study and the 3 in Boyet and Carlson [Boyet M. and Carlson R. W. (2007) A highly depleted Moon or a non-magma origin for the lunar crust? *Earth Planet. Sci. Lett.* **262**, 505–516] are reproducible, while static measurements in the previous two studies show analytical artifacts and cannot be used at the resolution of 10 ppm to determine a bulk Moon with either chondritic or superchondritic Sm/Nd ratios. The multidynamic data are best explained by a bulk Moon with a superchondritic Sm/Nd ratio that is similar to the present-day average for depleted MORB. Hafnium isotope data were collected on the same aliquots measured for their  $^{142}\text{Nd}/^{144}\text{Nd}$  isotope ratios in order to assess if

\* Corresponding author. Tel.: +1 2812446408.  
E-mail address: [alan.d.brandon@nasa.gov](mailto:alan.d.brandon@nasa.gov) (A.D. Brandon).

the correlation line for  $^{142}\text{Nd}$ – $^{143}\text{Nd}$  systematics reflect mixing processes or times at which lunar mantle sources formed. Based on the combined  $^{142}\text{Nd}$ – $^{143}\text{Nd}$ – $^{176}\text{Hf}$  obtained we conclude that the  $^{142}\text{Nd}$ – $^{143}\text{Nd}$  correlation line measured in this study is best interpreted as an isochron with an age of  $229^{+24}_{-20}$  Ma after the onset of nebular condensation. The uncertainties in the data permit the sources of these samples to have formed over a 44 Ma time interval. These new results for lunar mare basalts are thus consistent with a later Sm–Nd isotope closure time of their source regions than some recent studies have postulated, and a superchondritic bulk Sm/Nd ratio of the Moon and Earth. The superchondritic Sm/Nd signature was inherited from the materials that accreted to make up the Earth–Moon system. Although collisional erosion of crust from planetesimals is favored here to remove subchondritic Sm/Nd portions and drive the bulk of these bodies to superchondritic in composition, removal of explosive basalt material via gravitational escape from such bodies, or chondrule sorting in the inner solar system, may also explain the compositional features that deviate from average chondrites that make up the Earth–Moon system. This inferred superchondritic nature for the Earth similar to the modern convecting mantle means that there is no reason to invoke a missing, subchondritic reservoir to mass balance the Earth back to chondritic for Sm/Nd ratios. However, to account for the subchondritic Sm/Nd ratios of continental crust, a second superchondritic Sm/Nd mantle reservoir is required.

Published by Elsevier Ltd.

## 1. INTRODUCTION

Recent advancements in instrumentation that yield higher-precisions in the isotope ratio measurements of elements with atomic masses ranging from hydrogen to uranium have resulted in a renaissance for geochemistry and cosmochemistry. One fundamental result arising from the new technology is the recognition that terrestrial standards and modern samples representative of the Earth's convecting mantle show a *circa* 20 ppm difference in their  $^{142}\text{Nd}/^{144}\text{Nd}$  ratios relative to the average for ordinary and enstatite chondrites, which are thought to represent bulk solar system values (Boyet and Carlson, 2005; Andreasen and Sharma, 2006). The origins of this difference have important ramifications to models for nebular heterogeneity and bulk composition and evolution models for terrestrial bodies in the inner solar system. Coupled  $^{142}\text{Nd}$ – $^{143}\text{Nd}$  isotope systematics have also been used in a variety of materials to determine the differentiation timescales and evolution of terrestrial bodies in the first several hundred million years of the solar system history (e.g. Nyquist et al., 1995; Harper et al., 1995; Borg et al., 1999; Caro et al., 2003; Foley et al., 2005; Boyet and Carlson, 2005; Andreasen and Sharma, 2006; Caro et al., 2006; Rankenburg et al., 2007; Debaille et al., 2007; Bennett et al., 2007; Boyet and Carlson, 2007; Caro et al., 2008). These studies have documented that early differentiation leading to Sm/Nd ratios that are fractionated relative to average chondrites did occur during in the earliest histories of Earth, Mars, Moon, and the Eucrite Parent Body. The timing and mechanisms for such fractionation remain under debate.

Differences in  $^{142}\text{Nd}/^{144}\text{Nd}$  ratios in materials from terrestrial planets and the Moon depend on the cosmochemical history and the amount of Sm and Nd fractionation during early planetary differentiation. The isotope  $^{142}\text{Nd}$  is produced by two mechanisms. First,  $^{142}\text{Nd}$  is produced by the nucleosynthetic p-process in supernova events, and by the s-process in the interiors of some stars during their Red Giant phase, constituting approximately 4% and 96% of nucleosynthetic  $^{142}\text{Nd}$ , respectively (Anders and Grevesse, 1989; Wisshak et al., 1998; Arlandini et al., 1999). This comprises the bulk of  $^{142}\text{Nd}$  in our solar system. The heavier Nd isotopes ( $^{143}\text{Nd}$ ,  $^{144}\text{Nd}$ ,  $^{145}\text{Nd}$ ,  $^{146}\text{Nd}$ ,  $^{148}\text{Nd}$ , and  $^{150}\text{Nd}$ ) are produced by the s- and r-process, the latter of

which occurs in supernovae. Second,  $^{142}\text{Nd}$  is produced by  $^{146}\text{Sm}$  decay with a half-life of 103 Ma. Most of the  $^{146}\text{Sm}$  present in our solar system effectively decayed away by 500–600 Ma after the onset of nebular condensation (4.569 Ga, Bouvier et al., 2007), or 5–6 half-lives. Several estimates of the initial solar system  $^{146}\text{Sm}/^{144}\text{Sm}$  ratio are in the range of  $0.008 \pm 0.003$  (Nyquist et al., 1994; Amelin and Rotenberg, 2004; Caro et al., 2006; Jacobsen et al., 2008). The combination of the low abundance of  $^{146}\text{Sm}$ , its short half-life, and the magnitude of Sm/Nd fractionation that occurs in nebular and planetary processes (Caro et al., 2003; Amelin and Rotenberg, 2004; Caro et al., 2005; Debaille et al., 2008), means that abundance of  $^{142}\text{Nd}$  in materials resulting from  $^{146}\text{Sm}$  decay in the early solar system history ranges from 10 s to 100 s of ppm.

With these constraints on the isotopic variation of  $^{142}\text{Nd}/^{144}\text{Nd}$ , there is a  $\sim 20$  ppm difference between the average solar composition and modern day Earth materials. This difference may have resulted from 2 processes. One possibility is nebular materials that accreted to make the bulk Earth may have had a slightly higher Sm/Nd ratio than those materials that accreted to make average chondrites (Caro et al., 2008; Bourdon et al., 2008). An alternative possibility is that the bulk Earth has an identical  $^{142}\text{Nd}/^{144}\text{Nd}$  ratio to that of the average solar system but there is an early-formed missing or hidden reservoir with a subchondritic Sm/Nd ratio that offsets the  $\sim 20$  ppm higher  $^{142}\text{Nd}/^{144}\text{Nd}$  ratio observed in all measured terrestrial materials that are accessible relative to the average solar system. Where this 'missing reservoir' of material is now or whether this scenario is valid, is presently unknown. These scenarios for the materials that make up the Earth and specifically, its bulk Sm/Nd, have fundamental ramifications to nebular condensation and accretion models for the terrestrial planets.

An approach to constraining the bulk Sm/Nd ratio of the Earth is via coupled  $^{142}\text{Nd}/^{144}\text{Nd}$ – $^{143}\text{Nd}/^{144}\text{Nd}$  isotope ratio measurements of lunar mare basalts. This approach is ideal because the prevailing model for the origin of the Moon is by accretion of material expunged from the impact between a Mars-sized impactor and proto-Earth. Since rare-earth elements (REE) are refractory and do not fractionate between each other via volatile processing, the bulk

Sm/Nd ratio of the Earth and Moon should not have been modified by impact processes. The composition of the Earth and Moon, therefore, represents a hybrid mix between the two colliding bodies during the final stages of accretion (Halliday, 2000; Pahlevan and Stevenson, 2007). Because there was likely very efficient mixing between the proto-Earth and the impactor as evidenced by the indistinguishable isotopic compositions of Cr, K, O, and W (Humayun and Clayton, 1995; Lugmair and Shukolyukov, 1998; Wiechert et al., 2001; Touboul et al., 2007), and because REE are refractory and do not fractionate between each other via volatile processing, the bulk Sm/Nd of the Moon should also be identical to that of Earth following the accretion of the giant impactor. A pioneering study on the measurement of  $^{142}\text{Nd}/^{144}\text{Nd}$  isotope ratios (Nyquist et al., 1995) could not resolve this issue because of the imprecision of the data and it was not known at that time that young Earth materials and chondrites may possess distinct  $^{142}\text{Nd}/^{144}\text{Nd}$  compositions.

Two recent studies presenting high-precision  $^{142}\text{Nd}/^{144}\text{Nd}$ – $^{143}\text{Nd}/^{144}\text{Nd}$  isotope ratio measurements of lunar mare basalts have produced results that do not resolve whether the Moon had a chondritic or superchondritic bulk Sm/Nd with all of the ramifications each would have to the Earth–Moon system (Rankenburg et al., 2006; Boyet and Carlson 2007). Rankenburg et al. (2006) used a static measurement method to obtain high-precision Nd isotope data. They showed that the  $^{142}\text{Nd}$ – $^{143}\text{Nd}$  systematics for lunar mare basalts were strongly correlated and plotted on an isochron with an age of  $215 \pm 25$  Ma after the onset of nebular condensation. The isochron intersected the chondritic value for  $^{142}\text{Nd}/^{144}\text{Nd}$  at a  $^{147}\text{Sm}/^{144}\text{Nd}$  of 0.1964, identical to average chondrites. They argued that this was evidence for a Moon with a Sm/Nd ratio that was chondritic. In contrast, the data of Boyet and Carlson (2007) measured in static mode with three samples also re-measured separately using a multidynamic acquisition mode technique, define a trend using  $^{142}\text{Nd}$ – $^{143}\text{Nd}$  systematics that was generally displaced to higher  $^{142}\text{Nd}/^{144}\text{Nd}$  of up to 10–15 ppm relative to the trend of Rankenburg et al. (2006). Boyet and Carlson (2007) data gave an isochron age  $\sim 250$  Ma after the onset of nebular condensation similar to that in the Rankenburg et al. (2006) data. However, because the trend was displaced to higher  $^{142}\text{Nd}/^{144}\text{Nd}$ , the isochron intersected the terrestrial standard value for  $^{142}\text{Nd}/^{144}\text{Nd}$  at a superchondritic  $^{147}\text{Sm}/^{144}\text{Nd}$  ratio that is similar to the Earth's present-day convecting mantle. Comparing  $^{142}\text{Nd}$ – $^{143}\text{Nd}$  systematics for samples from the two different studies indicates that the discrepancy reflects differences in measured  $^{142}\text{Nd}/^{144}\text{Nd}$  ratios and may, in part, be related to analytical artifacts. The issue of whether the well-defined  $^{142}\text{Nd}$ – $^{143}\text{Nd}$  apparent isochrons in the lunar data have age implications for processes of the Moon is a matter of debate (Rankenburg et al., 2006; Boyet and Carlson, 2007; Caro et al., 2008; Bourdon et al., 2008). Rankenburg et al. (2006) suggested that the 215 Ma age represented closure of the mare basalt source regions upon cooling of a lunar magma ocean. In contrast, Boyet and Carlson (2007) suggested that the source of KREEP (K-, REE-, P-rich) lunar basalts formed as early as 110 Ma after the onset of nebular

condensation at 4.569 Ga, and that the sources of other mare basalts, such as for the Hi–Ti basalts, formed as late as 4.32 Ga through additional differentiation unrelated to a lunar magma ocean. In such a scenario, the apparent isochron for  $^{142}\text{Nd}$ – $^{143}\text{Nd}$  would represent a mixing line. This interpretation in part is a function of a less well-defined trend in the  $^{142}\text{Nd}$ – $^{143}\text{Nd}$  data (i.e. more scatter) than Rankenburg et al. (2006) obtained, allowing for a more complex early lunar evolution.

In this study, the six samples from Rankenburg et al. (2006) measured statically, were re-measured in two separate analytical campaigns using a multidynamic method for obtaining high-precision Nd isotope ratio measurements (Caro et al., 2006). The first objective is to use these data here to address issues of possible analytical artifacts in the previous two studies of Rankenburg et al. (2006) and Boyet and Carlson (2007). Second, the data are used to re-address the issue of how to best correct Nd isotope compositions of lunar mare basalt samples for cosmic-ray fluence. Third, the combined systematics of  $^{176}\text{Hf}$ – $^{142}\text{Nd}$ – $^{143}\text{Nd}$  are used to examine the mixing versus age significance of correlations defined by  $^{142}\text{Nd}/^{144}\text{Nd}$  and  $^{143}\text{Nd}/^{144}\text{Nd}$  isotope systematics, and to constrain the types of materials that constitute the Moon with implications for the Sm–Nd systematics of the Earth–Moon system.

## 2. ANALYTICAL TECHNIQUES

Procedures for chemical purification of Nd and high-precision measurements by thermal ionization mass spectrometry at the Isotope Laboratory of the Johnson Space Center (JSC) have been previously reported in detail (Rankenburg et al., 2006; Debaille et al., 2007, 2008; Bennett et al., 2007). A brief summary is presented here along with the details of the Hf isotope analytical protocols. Because of the potential issues surrounding previous  $^{142}\text{Nd}/^{144}\text{Nd}$  isotope ratio measurements for mare basalts, and to insure sample-spike equilibration between Lu and Hf, a more aggressive dissolution method than used in Rankenburg et al. (2006) was employed in the two analytical campaigns in this present investigation. Fractions of 7–160 milligrams of sample powders were dissolved using concentrated HF–HNO<sub>3</sub>–HCl in Parr digestion vessels. The amount of powder depended on obtaining a target amount of Nd for high-precision measurements of 400–1500 ng. These fractions were spiked with a mixed Lu–Hf spike prior to dissolution. In the first digestion, 1.5 ml of concentrated HF was added to sample powders and dissolved at 120 °C in 15 ml Savillex Teflon vials. After dry-down, the residues were dissolved in a mix of concentrated HF and HNO<sub>3</sub>, 3 ml and 0.75 ml, respectively, and transferred to the Parr vessels and heated for 72 h at 170 °C. After dry-down, the residues were taken up in 1.5 ml of concentrated HCl and heated for 72 h at 170 °C. After dry-down, the residues were taken up in 1.5 ml of 6 N HCl and 300 µl of concentrated perchloric acid in the Savillex vials at 120 °C for 24 h. Four more dissolutions followed in 1.5 ml 6 N HCl and the temperature was progressively increased from 120 °C to 150 °C to drive off perchloric acid during dry-down. Residues were re-dis-

solved in dilute HCl and clear solutions were obtained ensuring complete spike-sample equilibration for Lu and Hf. At this stage, for the first analytical campaign, including two replicates each of SAU-169 and 74275, a 5% (by volume) aliquot was extracted and spiked with a mixed Sm–Nd spike for isotope dilution abundance measurements. Because of the reproducibility between the aliquots of the homogenized powders (Table 1), no aliquots were removed for Sm–Nd spiking in the second analytical campaign. This campaign instead focused on assessing reproducibility of Nd isotope compositions.

Both the spiked and unspiked aliquots were put through ion exchange chromatography. In the first analytical campaign, the unspiked Sm–Nd cuts containing  $^{176}\text{Lu}$ – $^{178}\text{Hf}$  tracers, were put through a column with AG 1X8, 100–200 mesh anion resin to remove Fe using 6 M HCl as the elutant. The Hf–REE cut was put through this column a second time for additional purification. This cut was dried down, and taken up in a solution of 6 N HCl and  $\text{H}_2\text{O}_2$  and put through a column with LN-Spec resin to separate Hf + Zr from REE and some Ti. The Hf in the HFSE cut was then further purified with LN-Spec resin following

methods outlined in Münker et al. (2001). The REE cut was loaded in 2.5 N HCl, put through a column with AG 50 W  $\times$  8, 100–200 mesh cation resin, and collected with 6 N HCl. The REE fraction was separated using an LN-Spec column to separate Nd, Sm, and Lu. The Nd cut was further purified by solvent extraction to remove Ce (Rehkemper et al., 1996) followed by a cation exchange chromatography separation to remove Na that was introduced as sodium bromate in the solvent extraction procedure, followed by a second pass through the LN-Spec column. For the Sm–Nd spiked aliquots in the first analytical campaign, and the unspiked samples in the second analytical campaign, where no Lu and Hf were collected, the ion exchange procedure started with the cation column, and the anion and LN-Spec columns that preceded the cation column were not necessary. Procedural blanks for Nd, Sm, Lu, and Hf were <50 pg, <20 pg, <20 pg, and <80 pg, respectively. Blank corrections to spiked aliquots for these elements were  $\leq 0.2\%$ , and were negligible for the unspiked Nd aliquots.

The purified Sm and Nd cuts were loaded on outgassed Re filaments in phosphoric acid. A double filament configuration, one for ionization, one with the sample load for

Table 1

The Sm, Nd, Lu, Hf,  $^{143}\text{Nd}/^{144}\text{Nd}$  and  $^{176}\text{Hf}/^{177}\text{Hf}$  for the lunar basalts analyzed in this study. The measured  $^{143}\text{Nd}/^{144}\text{Nd}$  ratios were re-normalized using a LaJolla value in this study of 0.5118458 (Appendix A) to a value of 0.51186 (Amelin and Rotenberg, 2004). This corresponds to present-day chondrite uniform reservoir (CHUR) values of  $^{147}\text{Sm}/^{144}\text{Nd} = 0.1964$ , and  $^{143}\text{Nd}/^{144}\text{Nd} = 0.512637$ . The  $\epsilon^{143}\text{Nd}$  values are  $10^4$  parts deviation from the present-day average for CHUR. The  $\epsilon^{143}\text{Nd}$  corr., are corrected for neutron fluence using method described in the text. The  $\epsilon^{143}\text{Nd}_i$  values are corrected relative to CHUR at the time of crystallization for the ages listed. CHUR parameters for the Lu–Hf system used are  $^{176}\text{Lu}/^{177}\text{Hf} = 0.0336$  and  $^{176}\text{Hf}/^{177}\text{Hf} = 0.282785$  for Hf (Bouvier et al., 2008). The ‘-1’ and ‘-2’ designations at the end of the sample numbers correspond to separate fractions 1 and 2, respectively, for the samples listed. For 15386-1-2, the  $^{147}\text{Sm}/^{144}\text{Nd}$  ratio of 15386-1-2 was used to calculate initial  $\epsilon^{143}\text{Nd}$ . Both fractions came from the same 30 mg of homogenized powder. Crystallization ages for the samples in this study are from Rankenburg et al. (2006), Rankenburg et al. (2007), and references therein.

Sample	Wt. (mg)	Age (Ma)	Sm (ppm)	Nd (ppm)	$^{147}\text{Sm}/^{144}\text{Nd}$	$^{143}\text{Nd}/^{144}\text{Nd}$	$\pm 2\sigma$	$\epsilon^{143}\text{Nd}$	$\epsilon^{143}\text{Nd}$ corr.	$\epsilon^{143}\text{Nd}_i$
<i>KREEP</i>										
SAU169-1-1	7.07	3900	63.38	226.74	0.16910	0.5118145	0.0000013	-16.05	-15.93	-2.19
SAU 169-1-2	8.12	3900	51.69	184.86	0.16915	0.5118149	0.0000011	-16.04	-15.92	-2.21
15386-1-1	11.82	3850	31.60	112.70	0.16964	0.5118268	0.0000016	-15.81	-15.50	-2.21
15386-1-2	13.52	3850	–	–	–	0.5118236	0.0000008	-15.87	-15.56	-2.27
<i>Low-Ti</i>										
LAP 02205-1-1	80.07	2990	6.218	19.29	0.19499	0.5126349	0.0000009	-0.040	-0.005	0.54
15555-1-1	157.7	3320	2.567	7.811	0.19879	0.5128394	0.0000009	3.95	4.00	3.01
<i>High-Ti</i>										
70017-1-1	99.87	3690	6.239	14.66	0.25750	0.5143725	0.0000009	33.85	33.87	4.81
74275-1-1	40.25	3720	8.671	21.36	0.24816	0.5142493	0.0000008	31.45	31.47	6.67
74275-1-2	40.81	3720	8.033	19.57	0.24831	0.5142524	0.0000014	31.51	31.53	6.65
Sample	Wt. (mg)	Age (My)	Lu (ppm)	Hf (ppm)	$^{176}\text{Lu}/^{177}\text{Hf}$	$^{176}\text{Hf}/^{177}\text{Hf}$	$\pm 2\sigma^*$	<i>n</i>	$\epsilon^{176}\text{Hf}$	$\epsilon^{176}\text{Hf}_i$
<i>KREEP</i>										
SAU169-1-1	7.07	3900	7.363	50.21	0.02083	0.281726	0.0000009	5	-37.09	-3.49
SAU 169-1-2	8.12	3900	7.354	51.652	0.02022	0.281658	0.0000007	1	-39.49	-4.27
15386-1-1	11.82	3850	3.391	28.422	0.01695	0.281491	0.0000008	4	-45.40	-2.00
<i>Low-Ti</i>										
LAP 02205-1-1	80.07	2990	0.9100	5.490	0.02354	0.282501	0.0000006	7	-9.68	11.59
15555-1-1	157.7	3320	0.2760	2.221	0.01767	0.282152	0.0000008	6	-22.04	13.67
<i>High-Ti</i>										
70017-1-1	99.87	3690	1.184	8.574	0.01962	0.282133	0.0000006	7	-22.69	12.23
74275-1-1	40.25	3720	1.247	8.577	0.02065	0.282084	0.0000009	4	-24.44	8.13

\* Error is the weighted average of (*n*) repeated measurements of the sample solution.

evaporation, was used. The amount of Nd loaded for the unspiked high-precision runs ranged from 400–1500 ng for the samples and 600–900 ng for the standards. The amount of Sm loaded for the unspiked high-precision runs ranged from 75–200 ng for the samples and 60 ng for the standards. The Nd was measured on a 9-faraday cup ThermoFinnigan Triton thermal ionization mass spectrometer (TIMS), as positive metal ions. All measured data were corrected for instrumental mass fractionation using the exponential law and  $^{146}\text{Nd}/^{144}\text{Nd} = 0.7219$ . Cerium and Sm interferences on Nd were monitored using  $^{140}\text{Ce}$  and  $^{147}\text{Sm}$ . Corrections for  $^{142}\text{Ce}$  interference on  $^{142}\text{Nd}/^{144}\text{Nd}$  for both samples and standards ranged from 0.0 to 4.5 ppm (Appendix A). The isotope  $^{147}\text{Sm}$  was never above 1000 counts/s, and Sm interferences were negligible. All measurements were made following the multidynamic protocol of Caro et al. (2006), with rotating amplifiers between blocks. This procedure collects three lines of data for each cycle, where  $^{142}\text{Nd}$  is placed in cup L3, L2, and L1, respectively, with all other Nd isotopes placed accordingly in each line. Details of the methodology for this protocol are presented in Caro et al. (2006). Two standards were measured during the analytical campaign, an in-house Ames Nd standard, and the La Jolla Nd standard. These were alternately interspersed between sample runs during both analytical campaigns. Typical runs for both standards and samples were 4–6 V beams for  $^{142}\text{Nd}$  for 6–12 h consisting of 270–540 individual multidynamic cycles. Baselines were taken for 60 s between 10 multidynamic cycles that consisted of one block. The Triton virtual amplifier system allowed rotation of the amplifiers between cups before the beginning of each block to reduce bias. Gains were taken at the beginning of each run. The unspiked high-precision Sm isotope measurements were performed in static mode. Typical runs for both standards and samples were 4–6 V beams for  $^{154}\text{Sm}$  for 2 h consisting of 180 individual static cycles. Baselines were taken for 60 s between 10 static cycles that consisted of one block.

Isotopic analysis of Lu and Hf were performed on a GV Instruments *IsoProbe* at UW-Madison and data acquisition and reduction procedures followed those of Lapen et al. (2004). Samples and standards were measured on solutions with 30–40 ppb Hf and 20 ppb Lu. Sample introduction was through a 50  $\mu\text{L}/\text{min}$  nebulizer tip into a Cetac Aridus 2 desolvating nebulizer system. The total Hf sensitivity was  $\sim 340$  V/ppm. Repeated analysis of the JMC-475 Hf standard yielded  $^{176}\text{Hf}/^{177}\text{Hf} = 0.282163 \pm 0.000011$  ( $2\sigma$ ,  $n = 17$ ) over the course of this study and reproduced the accepted value for this standard ( $0.282163 \pm 0.000009$ , Blichert-Toft et al., 1997). Based on replicate analyses of spiked standard solutions and rock standards measured over the course of 9 years in the Wisconsin lab, the precisions of  $^{176}\text{Lu}/^{177}\text{Hf}$  isotope ratio measurements are  $\pm 0.2\%$ .

### 3. ACCURACY AND PRECISION OF $^{142}\text{Nd}/^{144}\text{Nd}$ MEASUREMENTS

Recent concerns over the accuracy of the precise  $^{142}\text{Nd}/^{144}\text{Nd}$  isotope ratio measurements of materials measured with the new generation TIMS (e.g. Triton), have

been raised (Caro et al., 2003; Caro et al., 2006; O'Neil et al., 2008; Upadhyay et al., 2008; Andreasen and Sharma, 2009). The first report of possible analytical artifacts affecting the  $^{142}\text{Nd}/^{144}\text{Nd}$  isotope ratio measurements at the internal and external precisions of  $\pm 6$  ppm ( $2\sigma$ ), was made by Caro et al. (2003). They observed that the range in  $^{142}\text{Nd}/^{144}\text{Nd}$  ratios over a range of for example,  $^{150}\text{Nd}/^{144}\text{Nd}$  for each cycle measured, did not strictly adhere to the exponential fractionation law employed to internally correct for instrumental mass bias for Nd isotopes. They derived a second-order mass bias correction to further correct the Nd isotope ratios in their work. These effects may have resulted from an optical aberration related to having a magnet placed in the ion-source. This group then switched from static measurements and removed the magnet from the ion-source. In this method  $^{142}\text{Nd}$  is typically measured in L3 and  $^{150}\text{Nd}$  in H4 (where the nine cups range in order on the low side from L4 to L1 to the axial, and on the high side from H1 to H4), to multidynamic measurements (Caro et al., 2006). They used a 3-line acquisition routine for high-precision isotope measurements, where  $^{142}\text{Nd}$  was measured in L3, L2, and L1,  $^{143}\text{Nd}$  in L2, L1, Axial, and so on. Caro et al. (2006) demonstrated precisions of  $\pm 2$ – $3$  ppm ( $2\sigma$ ) for the  $^{142}\text{Nd}/^{144}\text{Nd}$  ratio and instrumental mass bias that followed an exponential mass fractionation law with the multidynamic technique. A comprehensive description and analysis of this multidynamic method is presented in Caro et al. (2006) and need not be repeated here. Upadhyay et al. (2008) noted that, even in multidynamic measurements, artifacts may result in inaccurate  $^{142}\text{Nd}/^{144}\text{Nd}$  ratios at these precision levels. In particular, over the course of their runs, they observed periods of reverse fractionation where isotopically lighter, and hence, less fractionated Nd began to ionize and mix with isotopically heavier, and hence, more fractionated Nd. They attributed this to loads on the filaments that were acting as hybrid mixtures of distinct Nd reservoirs, such that different domains at different degrees of isotopic fractionation during ionization were emitting at variable rates and then mixing together to produce the bulk ion beam at any given time. Such effects have been observed prior to this during isotope analysis by thermal ionization (e.g., Hart and Zindler, 1989; Sharma and Chen, 2004). This effect results in more scatter of mass bias corrected individual  $^{142}\text{Nd}/^{144}\text{Nd}$  ratio integrations and average values that are higher than the true value. Upadhyay et al. (2008) found that this effect resulted in as great as 70 ppm shifts to higher average values during their analysis, as the hybrid mixtures deviated from the exponential instrumental mass fractionation law. Hence, these studies show several potential processes that can occur during Nd ionization in a TIMS that could lead to inaccurate values beyond the internal and external precisions of  $\pm 5$  ppm ( $2\sigma$ ) or better.

Within this context, the lunar mare basalt  $^{142}\text{Nd}/^{144}\text{Nd}$  data can be evaluated for accuracy given the discrepancies observed between those presented in Rankenburg et al. (2006) and those in Boyet and Carlson (2007), with direct comparisons to the new data presented here. It is noted that examination of each individual run for both the static data reported in Rankenburg et al. (2006) and the multidynamic

data on the same samples in this present study, show no evidence of reverse fractionation over the course of the runs with one exception noted below. All sample and standard runs show constant increasing  $^{146}\text{Nd}/^{144}\text{Nd}$  ratios versus time of the run. This is in contrast to the findings of Upadhyay et al. (2008) in their experiment, and in some cases for the measurements of O'Neil et al. (2008), where portions exhibiting reverse fraction in individual runs were clear evidence of complex domain mixing, and were discarded. Hence, deviations from the exponential law due to multi-domain Nd mixing that result in  $^{142}\text{Nd}/^{144}\text{Nd}$  values higher than the true value are not inherently obvious for the data obtained on the Triton at JSC. Raw data and plots for all runs can be sent for perusal upon request. As noted above for data from the JSC lab, one exception is sample 15555 from the Rankenburg et al. (2006) study that had reverse fractionation at the very end of the run. A regression through the  $^{142}\text{Nd}/^{144}\text{Nd}$  versus  $^{146}\text{Nd}/^{144}\text{Nd}$  shows a  $\sim 10$  ppm increase in the fractionation corrected  $^{142}\text{Nd}/^{144}\text{Nd}$  ratios with the degree of fractionation exemplified by the corresponding  $^{146}\text{Nd}/^{144}\text{Nd}$  ratio measurement. This is typical of many static runs with or without reverse fractionation, where drift of the average of fractionation corrected  $^{142}\text{Nd}/^{144}\text{Nd}$  occurs over the course of the run. This drift may be another possible bias in the data that may lead to the discrepancies observed between the static data measured on the JSC and DTM Tritons and may have its root cause in the processes discussed by Caro et al. (2006), Upadhyay et al. (2008), and Andreasen and Sharma (2009). However, because the JSC Triton static data from Rankenburg et al. (2006) is systematically lower than those from the DTM Triton (Boyet and Carlson, 2007), it does not appear that the JSC Triton data results from issues raised by Upadhyay et al. (2008) which produces higher than expected  $^{142}\text{Nd}/^{144}\text{Nd}$  isotope ratios.

As a means for evaluation of the possible effects of analytical artifacts, the data from the present study are examined and discussed by comparison to the data presented in Rankenburg et al. (2006) and Boyet and Carlson (2007). These comparisons are made on Nd isotope compositions that are uncorrected for neutron fluence and these corrections are discussed in Section 4. As noted in Section 4, because the neutron fluence imparted on different aliquots of the same samples analyzed in the two labs and the two distinct studies at JSC were identical, any differences observed for uncorrected Nd isotope ratios cannot result from this process. The strategy employed in this present study was to run the same six samples analyzed by Rankenburg et al. (2006) using the multidynamic method of Caro et al. (2006). Following Caro et al. (2006), the individual fractionation corrected ratios from each of the lines are summed together and statistics are performed on all of these ratios to arrive at the reported average values and internal precisions at  $\pm 2\sigma$  for the 'Multidynamic' averages reported in Tables 2 and 3. In the case for  $^{142}\text{Nd}/^{144}\text{Nd}$ ,  $^{143}\text{Nd}/^{144}\text{Nd}$ , and  $^{145}\text{Nd}/^{144}\text{Nd}$ , these isotopes were measured on each of the three lines and the final multidynamic values are the sums for all. For  $^{148}\text{Nd}/^{144}\text{Nd}$ ,  $^{148}\text{Nd}$  was only measured in lines 1 and 2 and the multidynamic values are the average for the two lines. For  $^{150}\text{Nd}/^{144}\text{Nd}$ ,  $^{150}\text{Nd}$

was only measured in line 1 and the static values are the average for this line only. The static measurements for each of lines 1–3 for  $^{142}\text{Nd}/^{144}\text{Nd}$  are also reported in Tables 2 and 3. This multidynamic method has been employed for the JSC Triton from 2007 to present (Debaille et al., 2007; Bennett et al., 2007; Debaille et al., 2009), with reproducible accuracy at  $\pm 3$  ppm ( $2\sigma$ ) on  $^{142}\text{Nd}/^{144}\text{Nd}$  for standards and samples. These data are reproducible with data for correlative Martian meteorites and Earth Hadean rocks published previously using the same multidynamic measurement technique (Caro et al., 2006; Caro et al., 2008).

Two distinct analytical campaigns were undertaken, where all six samples were measured in both campaigns using separate fractions put through the chemical purification methods. Individual sample analyses are each compared directly to standards only within each of the two distinct analytical campaigns. In the first campaign, standard data were taken over several months by two independent operators (Brandon, Bennett), when the faraday cups were new. The lunar basalt data was obtained in the middle of this campaign. For three of the samples in the first campaign, 2 separate aliquots were put through chemistry and measured independently for Nd. The Sm–Nd isotope dilution data for these samples are presented in Table 1. For the two separate fractions of SAU-169 and 74275, separate Sm–Nd spiked aliquots of the unspiked solutions were prepared. In the second analytical campaign, the six samples were again put through the chemistry to obtain pure Nd. Because this campaign focused on assessing reproducibility of the Nd isotopes only, no spiked aliquots were prepared. This campaign differed from the first campaign in that the standards were run over a restricted period that included the lunar basalt samples, and the cups were not moved over the course of the whole analytical period. This allows comparison between the two different approaches – the first campaign where standards are measured over several months and in between other uses of the instrument, versus more restricted periods where the instrument was dedicated only to high-precision isotope ratio measurement of Nd.

The multidynamic method of Caro et al. (2006) is advantageous not only because it empirically is shown to cancel or largely alleviate the possible effects observed in static runs as noted above, but also three separate static measurements are obtained that can be used to assess each run. All Nd isotope data obtained in this study are reported in the Appendix A including the static  $^{142}\text{Nd}/^{144}\text{Nd}$  isotope ratios for scans 1–3 and average Nd isotope ratios for the standards are reported in Table 2. All uncertainties quoted hereon are for  $\pm 2\sigma$ . The external precisions for the  $^{142}\text{Nd}/^{144}\text{Nd}$  ratio is better than or equal to  $\pm 2.7$  ppm for the Ames, La Jolla, and combined standard runs from the two analytical campaigns. All of the standard data combined yield  $^{142}\text{Nd}/^{144}\text{Nd} = 1.1418393 \pm 0.0000026$  ( $\pm 2.3$  ppm;  $n = 24$ ). This is comparable to the reproducibility for this method demonstrated by Caro et al. (2006), Debaille et al. 2009, and Bennett et al. (2007). Interestingly, each of the three lines in static mode are not reproducible between the two analytical campaigns. For line 1, the average for the combined Ames and La Jolla for  $^{142}\text{Nd}/^{144}\text{Nd} = 1.1418522 \pm 0.0000068$  for campaign 1,

Table 2

Summary of AMES and La Jolla Standard data for this study. The uncertainties listed are for  $\pm 2\sigma$  in the last (7th) decimal place. All individual analyses are listed in the [Appendix A](#).

Standard	$^{142}\text{Nd}/^{144}\text{Nd}$ Line 1 Static	$\pm 2\sigma$	$\mu^{142}\text{Nd}$	$\pm 2\sigma$ ppm	$^{142}\text{Nd}/^{144}\text{Nd}$ Line 2 Static	$\pm 2\sigma$	$\mu^{142}\text{Nd}$	$\pm 2\sigma$ ppm	$^{142}\text{Nd}/^{144}\text{Nd}$ Line 3 Static	$\pm 2\sigma$	$\mu^{142}\text{Nd}$	$\pm 2\sigma$ ppm
AMES Campaign 1 $n = 10$	1.1418298	60	0.9	5.3	1.1418519	64	-0.2	5.6	1.1418327	54	-1.3	4.7
LaJolla Campaign 1 $n = 5$	1.1418267	82	-1.8	7.2	1.1418527	81	0.4	7.1	1.1418371	37	2.6	3.3
All Campaign 1 $n = 15$	1.1418288	72	0.0	6.3	1.1418522	68	0.0	5.9	1.1418342	64	0.0	5.6
AMES Campaign 2 $n = 7$	1.1418485	82	0.5	7.2	1.1418262	125	-1.1	11.0	1.1418394	94	0.8	8.2
LaJolla Campaign 2 $n = 2$	1.1418461	107	-1.6	9.4	1.1418318	20	3.8	1.7	1.1418353	82	-2.8	7.2
All Campaign 2 $n = 9$	1.1418479	83	0.0	7.3	1.1418274	119	0.0	10.4	1.1418385	93	0.0	8.2
Standard	$^{142}\text{Nd}/^{144}\text{Nd}$ Multidynamic	$\pm 2\sigma$	$\mu^{142}\text{Nd}$	$\pm 2\sigma$ ppm	$^{143}\text{Nd}/^{144}\text{Nd}$ Multidynamic	$\pm 2\sigma$	$\mu^{143}\text{Nd}$	$\pm 2\sigma$ ppm	$^{145}\text{Nd}/^{144}\text{Nd}$ Multidynamic	$\pm 2\sigma$	$\mu^{145}\text{Nd}$	$\pm 2\sigma$ ppm
AMES Campaign 1 $n = 10$	1.1418389	28	-0.3	2.5	0.5121337	12	-0.01	2.4	0.34840527	03	0.4	3.7
LaJolla Campaign 1 $n = 5$	1.1418393	11	0.0	0.9	0.5118458	09	-5.63	1.8	0.34840488	17	-0.7	4.8
All Campaign 1 $n = 15$	1.1418391	24	-0.2	2.1					0.34840514	14	0.0	4.1
AMES Campaign 2 $n = 7$	1.1418400	31	0.6	2.7	0.5121346	12	0.01	2.4	0.34840292	06	0.4	1.7
LaJolla Campaign 2 $n = 2$	1.1418391	10	-0.3	0.9	0.5118461	06	-5.62	1.1	0.34840225	01	-1.5	0.4
All Campaign 2 $n = 9$	1.1418398	28	0.4	2.5					0.34840277	08	0.0	2.3
All Standards $n = 24$	1.1418393	26	0.0	2.3								
Standard	$^{148}\text{Nd}/^{144}\text{Nd}$ Multidynamic	$\pm 2\sigma$	$\mu^{148}\text{Nd}$	$\pm 2\sigma$ ppm	$^{150}\text{Nd}/^{144}\text{Nd}$ Static	$\pm 2\sigma$	$\mu^{150}\text{Nd}$	$\pm 2\sigma$ ppm				
AMES Campaign 1 $n = 10$	0.2415790	16	1.2	6.7	0.2364506	54	0.2	22.7				
AMES Campaign 2 $n = 7$	0.2415784	09	-1.7	3.5	0.2364505	19	-0.3	8.1				
All AMES 1 $n = 17$	0.2415788	15	0.0	6.2	0.2364506	42	0.0	17.7				
LaJolla Campaign 1 $n = 5$	0.2415814	20	11.1	8.2	0.2364549	37	18.2	15.5				
LaJolla Campaign 2 $n = 2$	0.2415803	06	6.4	2.3	0.2364544	14	16.2	6.0				
All LaJolla $n = 7$	0.2415811	20	9.8	8.2	0.2364547	31	17.6	13.0				

and  $^{142}\text{Nd}/^{144}\text{Nd} = 1.14182744 \pm 0.0000119$  for campaign 2. Similar shifts are observed in the static data in Lines 2 and 3 for  $^{142}\text{Nd}/^{144}\text{Nd}$  between the two campaigns (Table 2). These shifts that occur with aging cups do not appear to largely affect the multidynamic measurements perhaps as a result of the dynamic analysis cancelling the effects of Faraday collector efficiencies. The averages for multidynamic  $^{143}\text{Nd}/^{144}\text{Nd}$  for Ames and LaJolla between the two analytical campaigns are indistinguishable at the external precision for the average of all standards for both campaigns of  $\pm 2.3$  ppm as noted above (Table 2). However, for multidynamic  $^{145}\text{Nd}/^{144}\text{Nd}$  ratios, the standard averages are  $0.3480514 \pm 0.0000014$  ( $\pm 4.1$  ppm) and  $0.34840277 \pm 0.0000008$  ( $\pm 2.3$  ppm) corresponding to a difference of 6.8 ppm and slightly outside of  $2\sigma$  external precision (Table 2). The averages for multidynamic  $^{148}\text{Nd}/^{144}\text{Nd}$  and static  $^{150}\text{Nd}/^{144}\text{Nd}$  ( $^{150}\text{Nd}$  is only measured in Line 1) for Ames Nd are indistinguishable between

the two analytical campaigns, as are the La Jolla averages. However, the combined average for La Jolla from both campaigns relative to the combined average for Ames Nd is 9.9 and 17.6 ppm higher for  $^{148}\text{Nd}/^{144}\text{Nd}$  and  $^{150}\text{Nd}/^{144}\text{Nd}$ , respectively. A similar result was found by O'Neil et al. (2008) and thus, this confirms that  $^{148}\text{Nd}/^{144}\text{Nd}$  and  $^{150}\text{Nd}/^{144}\text{Nd}$  are anomalous for the La Jolla standard and all normalization for these two ratios should be relative to the Ames or terrestrial standards which have been shown to have identical  $^{148}\text{Nd}/^{144}\text{Nd}$  and  $^{150}\text{Nd}/^{144}\text{Nd}$  isotope ratios (Debaille et al., 2007; Bennett et al., 2007). The differences between La Jolla and Ames Nd likely reflect real measured differences in the stable isotope composition of these two standards (O'Neil et al., 2008).

As there were relatively large differences between the static measurements in Line 1, Line 2, and Line 3 for the  $^{142}\text{Nd}/^{144}\text{Nd}$  ratio, and a small difference in the multidy-

Table 3

$^{142}\text{Nd}/^{144}\text{Nd}$  isotope data for the lunar basalts measured in this study with no neutron fluence corrections. The uncertainties listed are for  $\pm 2\sigma$  in the last (7th) decimal place. Samples with ‘-1’ and ‘-2’ designations following the sample name, are from Analytical Campaign 1 and Campaign 2, respectively, and normalized relative to the averages for the standards in Table 2. Samples with ‘-1’ and ‘-2’ and ‘-3’ designations following the Campaign designations are for separate fractions of each sample measured, and ‘rpt’ is a repeat measurement for a sample. See Appendix A for complete Nd data set.

Sample	$\mu^{142}\text{Nd}$ Line 1 Static	$\pm 2\sigma$ ppm	$\mu^{142}\text{Nd}$ Line 2 Static	$\pm 2\sigma$ ppm	$\mu^{142}\text{Nd}$ Line 3 Static	$\pm 2\sigma$ ppm	$\mu^{142}\text{Nd}$ Multidynamic	$\pm 2\sigma$ ppm	$\mu^{143}\text{Nd}$ Multidynamic	$\pm 2\sigma$ ppm	$\mu^{145}\text{Nd}$ Multidynamic	$\pm 2\sigma$ ppm	$\mu^{148}\text{Nd}$ Multidynamic	$\pm 2\sigma$ ppm	$\mu^{150}\text{Nd}$ Static	$\pm 2\sigma$ ppm
<i>KREEP</i>																
SAU169-1-1	-31.3	5.3	-18.9	5.1	-24.1	5.4	-25.4	2.9	-6.52	2.5	-5.9	2.6	7.2	4.6	13.3	9.3
SAU 169-1-2	-27.0	3.5	-24.1	3.7	-22.6	3.8	-25.4	2.2	-6.51	2.1	-7.6	1.7	1.8	3.3	4.0	7.2
SAU 169-2-3	-23.5	4.0	-21.0	3.8	-32.0	3.8	-27.8	1.9	-6.56	1.8	-6.2	1.7	-3.1	3.3	2.3	7.2
SAU 169-2-3.rpt	-21.8	3.9	-23.5	4.0	-31.6	3.9	-26.8	2.1	-6.57	1.8	-9.1	1.7	-7.3	2.9	-10.4	6.8
Average	-25.9	8.4	-21.9	4.8	-27.6	9.9	-26.3	2.4	-6.5	6.5	-7.2	2.9	-0.3	12.5	2.3	19.5
15386-1-1	-30.9	6.8	-26.8	7.7	-27.6	8.4	-30	4.2	-6.28	3.1	-12.2	3.7	-9.4	4.6	-30.3	14.0
15386-1-2	-34.2	3.2	-23.4	3.1	-32.0	3.0	-31	1.8	-6.34	1.6	-14.8	1.4	-2.3	2.9	1.8	5.9
15386-2-3	-29.3	3.9	-32.0	3.9	-26.8	3.9	-31.9	2.2	-6.47	1.6	-16.3	1.7	-5.2	3.3	7.3	7.2
15386-2-3.rpt	-30.2	3.8	-29.6	3.8	-35.3	3.6	-31.3	2.1	-6.44	1.6	-16.6	1.7	-5.6	2.9	11.1	6.3
Average	-31.2	4.3	-27.9	7.4	-30.4	7.9	-31.1	1.6	-6.4	18.2	-14.9	4.0	-5.6	5.8	-2.5	37.9
<i>Low-Ti</i>																
LAP 02205-1-1	-9.7	3.2	-2.2	3.9	-10.3	3.2	-8.9	1.9	9.50	1.8	1.0	1.7	1.0	3.3	-0.7	5.9
LAP 02205-2-2	-6.5	3.9	-0.3	3.8	-14.7	4.1	-8.1	2	9.48	1.8	0.4	1.7	-3.6	3.3	5.6	6.3
LAP 02205-2-2.rpt	-3.1	3.9	-3.1	4.3	-14.8	3.9	-8.2	1.9	9.48	1.8	-1.4	2.0	-1.5	2.9	9.0	6.3
Average	-6.4	6.6	-1.9	2.9	-13.2	5.1	-8.4	0.8	9.5	2.8	0.0	2.5	-1.3	4.6	4.7	9.9
15555-1-1	-6.8	3.3	-1.0	3.5	-7.0	3.7	-3.7	1.8	13.50	1.6	-2.4	1.4	4.3	2.5	9.9	5.5
15555-2-2	-2.4	3.9	-11.2	3.7	-12.6	3.8	-8.1	2.1	13.40	1.8	-1.6	2.0	-0.7	2.9	1.8	7.2
Average	-4.6	6.3	-6.1	14.4	-6.8	7.9	-5.9	6.2	13.4	13.0	-2.0	1.1	1.8	7.0	5.9	11.4
<i>High-Ti</i>																
70017-1-1	10.7	3.9	18.0	4.3	13.6	3.5	13.7	1.8	43.43	1.8	0.2	1.7	1.0	2.9	5.6	6.3
70017-2-2	9.3	4.0	13.4	4.1	10.7	4.0	13.1	2.3	43.43	2.0	-2.2	1.7	0.2	2.9	7.3	7.2
Average	10.0	1.9	15.7	6.5	12.2	4.1	13.4	0.9	43.4	0.3	-1.0	3.4	0.6	1.2	6.5	2.4
74275-1-1	14.5	3.7	23.2	3.7	17.8	3.6	17	1.9	41.03	1.8	1.0	1.7	2.2	3.3	4.0	6.3
74275-1-2	15.5	5.8	17.7	5.4	13.9	5.5	15.3	3	41.08	2.0	-1.3	2.3	7.6	5.0	5.2	8.9
74275-2-3	19.2	5.1	17.5	5.1	16.9	5.1	16.5	2.8	41.06	2.0	-2.3	2.3	1.0	4.1	19.2	8.0
Average	16.4	5.0	19.4	6.5	16.2	4.1	16.2	1.8	41.1	5.9	-0.8	3.4	3.6	7.0	9.5	16.9

dynamic  $^{145}\text{Nd}/^{144}\text{Nd}$  ratio between the two analytical campaigns, all of the lunar mare basalt Nd isotope data are averaged relative to the standard values of the analytical campaign in which each was measured in. This allows for direct comparison of the normalized results between the two analytical campaigns in  $\epsilon$  notation for  $^{143}\text{Nd}$  ( $10^4$  parts deviation from the standard average) and  $\mu$  notation for  $^{142}\text{Nd}$  and  $^{145}\text{Nd}$  ( $10^6$  parts deviation from the standard average). Using this normalization technique versus taking a combined average for all standards measured in both analytical campaigns results in no systematic differences greater than 1 ppm for lunar mare basalts  $\mu^{142}\text{Nd}$  values.

The high-precision Nd isotope compositions for unspiked fractions of the lunar mare basalts, each representing 2–3 distinct fractions processed and 2–4 distinct measurements, are listed in Table 3. In all cases, with the exception of 15555, the averages for multidynamic  $\mu^{142}\text{Nd}$  for each sample have  $\pm 2\sigma$  uncertainties from 0.8 to 2.4 ppm, better than or comparable to the external precision for the standard average at  $\pm 2.3$  ppm. The average for two fractions of 15555 run in the two analytical campaigns has a  $\pm 2\sigma$  uncertainty of 6.2 ppm. The complete range from KREEP to Hi-Ti basalts for the six samples from  $\mu^{142}\text{Nd}$  of  $-31$  to  $+16$  is comparable to the range observed for mare basalts in Rankenburg et al. (2006) and Boyet and Carlson (2007).

In Fig. 1A, the combined averages for the  $^{142}\text{Nd}/^{144}\text{Nd}$  ratio (using  $\mu^{142}\text{Nd}$  notation) for the lunar mare basalts, are plotted. The averages for  $\mu^{142}\text{Nd}$  for static Line 1, Line 2, and Line 3, all plot along a 1:1 line with multidynamic  $\mu^{142}\text{Nd}$  for each for the six sample averages, at a level of  $\pm 6$  ppm or better. Given that the external precisions for the averages of the standards for the static measurements for each line ranges from  $\pm 5.6$  to  $\pm 10.4$  ppm (Table 2), this indicates complete correlation between static  $^{142}\text{Nd}/^{144}\text{Nd}$  and multidynamic  $^{142}\text{Nd}/^{144}\text{Nd}$  for the standards and the lunar mare basalt sample measurements in this study.

In Fig. 1B, the averages for the multidynamic measurements for  $\mu^{142}\text{Nd}$  for this study and from Boyet and Carlson (2007) are compared to the averages for independent static measurements of the same samples from the JSC Triton (Rankenburg et al. 2006) and the DTM Triton (Boyet and Carlson, 2007), respectively. For the JSC data the averages for the static measurements of each sample from the earlier Rankenburg et al. (2006) study plot as a well-correlated line ( $R^2=0.99$ ) with the averages of the multidynamic measurements of this study (Table 3). However, the correlation is not 1:1. The KREEP samples SAU-169 and 15386 plot within uncertainty between the two data sets, while the Lo-Ti LAP 002205 and 15555, and Hi-Ti 70017 and 74275 samples have increasingly lower  $\mu^{142}\text{Nd}$  relative to the multidynamic measurements from this study. For the DTM data, while only three measurements are available for comparison, the averages for the static measurements of each sample plot as a well-correlated line ( $R^2 = 0.99$ ) with the averages of the multidynamic measurements on separate fractions of this study (Boyet and Carlson, 2007). However, the DTM data also do not correlate along a 1:1 line. The Hi-Ti sample 70017 is within uncertainty between the two data sets, while with decreasing  $\mu^{142}\text{Nd}$  the static

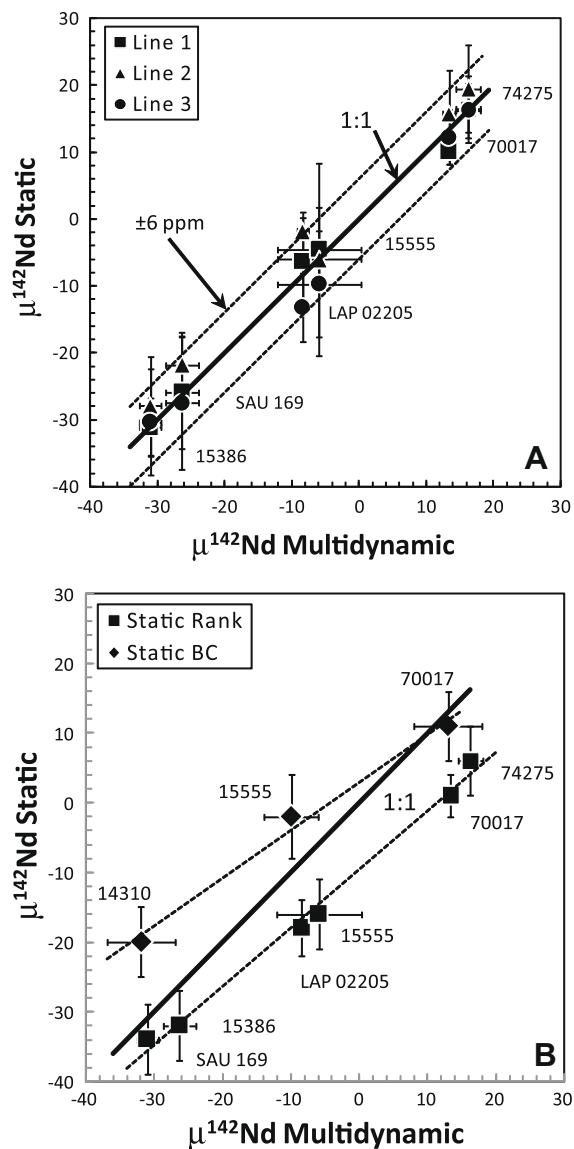


Fig. 1. (A) Averages for  $\mu^{142}\text{Nd}$  static measurements for Lines 1–3 plotted versus the average  $\mu^{142}\text{Nd}$  multidynamic for the six samples measured in this study (Table 3). All average data are normalized to the standards in Table 2 for each of the distinct analytical campaigns. The averaged data for all six samples combined follow a 1:1 correlation within  $\pm 6$  ppm as shown. Error bars are  $2\sigma$ . (B) The averages for the  $\mu^{142}\text{Nd}$  static measurements from Rankenburg et al. (2006) (Rank) are plotted versus the averages for the  $\mu^{142}\text{Nd}$  multidynamic for the correlative samples measured in this study and on the same Triton at JSC. The averages for the  $\mu^{142}\text{Nd}$  static measurements from Boyet and Carlson (2007) (BC) are plotted versus the averages for the  $\mu^{142}\text{Nd}$  multidynamic for the correlative samples measured in their study and on the same Triton at DTM. Regression lines for each comparison are shown, as are a 1:1 line. Error bars are  $2\sigma$ .

measurements are larger compared to the multidynamic measurements. For each of the JSC and DTM datasets, the largest discrepancies between static and multidynamic measurements are  $-12.4$  (70017) and  $+12.4$  (14310) ppm, respectively, much larger than the established  $2\sigma$  external

precisions for all four data sets. Importantly, the multidynamic measurements for Lo–Ti sample 15555 and Hi–Ti sample 70017 from JSC and DTM are within analytical uncertainties of each other (Fig. 1B). The KREEP impact melt 14310 measured in multidynamic mode at DTM is within uncertainty of the two KREEP samples SAU 169 and 15386 measured in multidynamic mode at JSC.

In summary, these comparisons show that within the sparse lunar mare data set obtained to present, the multidynamic measurements from JSC and DTM are reproducible. In contrast, static measurements between labs are not reproducible nor are they reproducible as compared to the multidynamic isotope ratios. The origins of the differences between static and multidynamic data are unknown but it must reflect some type of analytical artifact associated with the static measurements. In order to compare the origins of Sm–Nd variations between the Earth, Moon, and chondrites a precision of  $\pm 5$  ppm or better on  $\mu^{142}\text{Nd}$  values is required and therefore we recommend against using  $^{142}\text{Nd}/^{144}\text{Nd}$  ratios measured using a static analysis. Hence, with the exception of a discussion of neutron fluence effects in Section 4, only high-precision multidynamic Nd isotope data is considered which includes the averages for the multidynamic  $\mu^{142}\text{Nd}$  of the samples reported in this study, and the three multidynamic  $\mu^{142}\text{Nd}$  from Boyet and Carlson (2007).

#### 4. NEUTRON FLUENCE CORRECTIONS ON Nd ISOTOPES

Nyquist et al. (1995) established a correction method for Nd isotopes for the effects of cosmic-ray exposure interactions for material at or near the surface of an airless body that was based on the work of Lingenfelter et al. (1972). The method takes advantage of using an isotope with a large effective thermal neutron absorption cross section ( $\sigma_{\text{eff}}$ ) for an element similar to Nd, to measure the relative neutron doses for each sample and apply a correction. For  $^{149}\text{Sm}(n,\gamma)^{150}\text{Sm}$ , the  $^{149}\text{Sm}$   $\sigma_{\text{eff}}$  is more than  $10^3$  times larger than those for all 7 Nd isotopes. Several studies have now shown a correlation between negative  $\epsilon^{149}\text{Sm}$  and positive  $\epsilon^{150}\text{Sm}$  in lunar mare basalts verifying the effect of neutron capture from cosmic-ray exposure (Lugmair and Marti, 1971; Nyquist et al., 1995; Rankenburg et al., 2006; Boyet and Carlson, 2007). In the present study, unspiked fractions of samples in the first analytical campaign were measured for high-precision Sm isotopic compositions (Table 4). The new Sm lunar mare basalt and standard data are reproducible within uncertainty to those previously obtained. Internal precision on  $\epsilon^{149}\text{Sm}$  ( $10^4$  parts variation relative to the Ames Sm terrestrial standard) for individual measurements in this study is better than  $\pm 0.06$  ( $2\sigma$ ). The individual samples and the Ames standard for this study and those from Rankenburg et al. (2006) measured on the same Triton at JSC reproduce at an external  $\epsilon^{149}\text{Sm}$  of  $\pm 0.5$  ( $2\sigma$ ) (Table 4). These values compare well with the same samples measured by Nyquist et al. (1995) and Boyet and Carlson (2007). For example, for sample 15386, two fractions in this study have  $\epsilon^{149}\text{Sm}$  of  $-32.1$  and  $-32.3$ , respectively. Nyquist et al. (1995) and Rankenburg et al.

Table 4

The Sm isotope data measured in this study, measured from August 1 to August 12, 2008. Standard data is compiled for the JSC Triton for the analytical campaign. All ratios normalized to  $^{147}\text{Sm}/^{152}\text{Sm} = 0.560828$ . The uncertainties listed are for  $\pm 2\sigma$  in the last (6th) decimal place. Averages for the Sm standard are listed from Rankenburg et al. (2006).

Moon	$^{144}\text{Sm}/^{152}\text{Sm}$	$\pm 2\sigma$	$^{148}\text{Sm}/^{152}\text{Sm}$	$\pm 2\sigma$	$^{149}\text{Sm}/^{152}\text{Sm}$	$\pm 2\sigma$	$\epsilon_{149}$	$^{150}\text{Sm}/^{152}\text{Sm}$	$\pm 2\sigma$	$\epsilon_{150}$	$^{154}\text{Sm}/^{152}\text{Sm}$	$\pm 2\sigma$
<i>KREEP</i>												
SAU169 1-1	0.114991	1	0.420466	2	0.516230	2	-12.4	0.276642	1	+23.3	0.850798	04
SAU169 1-2	0.114989	1	0.420467	2	0.516235	2	-12.3	0.276642	1	+23.3	0.850673	10
15386 1-1	0.114987	1	0.420481	2	0.515212	2	-32.1	0.277686	1	+61.1	0.850782	05
15386 1-2	0.115007	2	0.420468	2	0.515199	2	-32.3	0.277663	2	+60.3	0.850823	05
<i>Low-Ti</i>												
LAP_02205 1-1	0.114998	2	0.420445	2	0.516676	2	-3.8	0.276158	2	+5.8	0.850708	06
15555 1-1	0.115994	2	0.420453	2	0.516577	2	-5.7	0.276269	1	+9.8	0.850717	05
<i>High-Ti</i>												
70017 1-1	0.114986	1	0.420449	2	0.516769	2	-2.0	0.276075	1	+2.8	0.850760	04
74275 1-1	0.114983	2	0.420455	2	0.516785	2	-1.6	0.276095	2	+3.5	0.850772	05
74275 1-2	0.114985	2	0.420454	2	0.516764	2	-2.0	0.276084	2	+3.1	0.850771	05
Average	0.114991	15	0.420460	23							0.850756	95
<i>AMES standard</i>												
AMES standard	$^{144}\text{Sm}/^{152}\text{Sm}$	$\pm 2\sigma$	$^{148}\text{Sm}/^{152}\text{Sm}$	$\pm 2\sigma$	$^{149}\text{Sm}/^{152}\text{Sm}$	$\pm 2\sigma$	$\epsilon_{149}$	$^{150}\text{Sm}/^{152}\text{Sm}$	$\pm 2\sigma$	$\epsilon_{150}$	$^{154}\text{Sm}/^{152}\text{Sm}$	$\pm 2\sigma$
Run 1	0.114985	2	0.420453	2	0.516872	2	+0.04	0.275999	2	+0.24	0.850771	05
Run 2	0.114979	2	0.420448	2	0.516867	2	-0.06	0.275997	2	-0.24	0.850773	05
Average $n = 2$	0.114982	9	0.420450	6	0.516870	7	0.0	0.275998	2		0.850772	03
Rankenburg $n = 5$	0.114985	6	0.420454	7	0.516864	9	-0.12	0.275997	3		0.850781	13

(2006) obtained values of  $-31.6$  and  $-32.5$ , respectively. In this study, sample 15555 has  $\epsilon^{149}\text{Sm}$  of  $-5.7$ , and values of  $-5.0$  and  $-4.9$ ,  $-5.3$ ,  $-6.2$  and  $-5.6$ , were obtained by Nyquist et al. (1995), Rankenburg et al. (2006), and Boyet and Carlson (2007), respectively. Similar overlapping values were obtained where the same samples were measured at better than  $\pm 0.5 \times \epsilon^{149}\text{Sm}$  units consistent with the reproducibility of the standard between the different studies. This indicates that among the sample fractions of lunar mare basalts distributed to the individual groups for analyses, the effects of neutron fluence on Sm isotopes is identical for a given rock at a level where the small differences measured will not impart differences in Nd isotope correction methods of  $>0.25$  ppm (Nyquist et al., 1995).

Nyquist et al. (1995) and Rankenburg et al. (2006) present comprehensive discussions on using the measured  $\epsilon^{149}\text{Sm}$  values to correct Nd isotopes for neutron fluence effects. In brief, the neutron flux any lunar sample received can be calculated using measured  $\epsilon^{149}\text{Sm}$  using Equation 2 of Nyquist et al. (1995):

$$\epsilon^{149}\text{Sm} = -1 \times 10^4 \sigma_{\text{eff}} \Psi \quad (1)$$

where  $\sigma_{\text{eff}}$  is the effective thermal neutron cross section in  $\text{cm}^2$ , and  $\Psi$  is the thermal neutron flux in  $\text{n/cm}^2$ . Hence, solution of  $\Psi$  will depend on the  $\sigma_{\text{eff}}$  of  $^{149}\text{Sm}$  for any measured  $\epsilon^{149}\text{Sm}$ . This method is independent of the composition of the sample. Once the amount of thermal and epithermal neutron flux is calculated, these can then be applied to calculate the isotopic shift to each Nd isotope for each sample using equations in Nyquist et al. (1995) and applying exponential law fractionation corrections to the correction factors.

An unresolved issue is the accurate value of  $\sigma_{\text{eff}}$  for  $^{149}\text{Sm}$ , because changes in this value results in proportional shifts in the amount of  $\Psi$  (Boyet and Carlson, 2007). This in turn results in significant changes in the correction to each Nd isotope. Table 5 and Fig. 2 show the corrected  $^{142}\text{Nd}/^{144}\text{Nd}$  isotopic compositions (as  $\mu^{142}\text{Nd}$  corr) and extent of the  $^{142}\text{Nd}$  correction in ppm, respectively, for samples from the present study and those from Boyet and Carlson (2007) with  $\sigma_{\text{eff}}$  values used in previous studies (Nyquist et al., 1995; Rankenburg et al., 2006; Boyet and Carlson, 2007). In this study,  $^{145}\text{Nd}$  is used as an independent test for the corrections applied to  $^{142}\text{Nd}$ , and was chosen in part because the  $^{145}\text{Nd}/^{144}\text{Nd}$  ratio is the most accurately determined ratio with no radiogenic input besides  $^{142}\text{Nd}/^{144}\text{Nd}$ , when the data are internally normalized to  $^{146}\text{Nd}/^{144}\text{Nd} = 0.7219$  with an exponential instrumental mass fractionation law. In addition,  $^{145}\text{Nd}(n,\gamma)^{146}\text{Nd}$  has a epithermal resonance integral of 231 barns, a factor of 10 larger than  $^{142}\text{Nd}$ ,  $^{144}\text{Nd}$ , or  $^{146}\text{Nd}$ . As shown below, this is a sensitive indicator of the accurately applied epithermal neutron flux ( $\Xi$ ) and  $\Psi/\Xi$  ratio used in the calculations. The production of  $^{146}\text{Nd}$  from neutron absorption of  $^{145}\text{Nd}$  also affects the internal mass fractionation normalization ratio ( $^{146}\text{Nd}/^{144}\text{Nd}$ ) that results in inaccurately applied corrections to all other Nd isotopes. It is critical that any correction applied to all Nd isotopes should result in  $\mu^{145}\text{Nd}$  within uncertainty of the terrestrial standard. Hence, the extent of  $\Xi$  a sample received is also a factor. Direct

measurements were made of lunar soil in the Apollo 17 Lunar Neutron Probe Experiment (LNPE, Woolum et al., 1975). They obtained a  $\Psi/\Xi$  of  $1.1 \pm 0.2$  at  $180 \text{ g/cm}^2$ , and this provides the best estimate at present on the amount of thermal relative to epithermal neutron flux. Nyquist et al. (1995) derived a range of  $\Psi/\Xi$  from 0.3 to 3.0 for individual samples based on a non-linear regression model of measured Sm isotope ratios and tabulated thermal neutron cross sections and epithermal resonance integrals from nuclear data available at that time. It is unclear how much uncertainty is associated with this range.

For samples that were exposed to relatively large neutron fluxes and have consequently large negative  $\epsilon^{149}\text{Sm}$  anomalies, the corrections to  $\mu^{142}\text{Nd}$  can be 35 ppm or more, depending on the values of  $\sigma_{\text{eff}}$  and  $\Psi/\Xi$  (Fig. 2). Such large differences in the corrected  $\mu^{142}\text{Nd}$  strongly affect the interpretation of the lunar mare basalt data. Rankenburg et al. (2006) calculated  $^{149}\text{Sm}$   $\sigma_{\text{eff}}$  to be 71,267 barns ( $10^{-24} \text{ cm}^2$ ). This was calculated for a Maxwellian averaged cross section over a thermal energy interval of  $10^{-5}$  to 0.5 eV and used the most recent nuclear data compiled in the JEFF-3.1 library and the INTER, LINEAR, and RECENT codes ([www.nea.fr/html/dbdata/JEFF/](http://www.nea.fr/html/dbdata/JEFF/)). This method was also used by Rankenburg et al. (2006) to calculate the thermal cross sections for  $^{141}\text{Pr}$  (11.5 barns),  $^{142}\text{Nd}$  (18.6 barns),  $^{143}\text{Nd}$  (335 barns),  $^{144}\text{Nd}$  (3.6),  $^{145}\text{Nd}$  (41.9),  $^{146}\text{Nd}$  (1.4 barns), and epithermal resonance integrals for  $^{149}\text{Sm}$  (3486 barns),  $^{141}\text{Pr}$  (17.9 barns),  $^{142}\text{Nd}$  (6.1 barns),  $^{143}\text{Nd}$  (132 barns),  $^{144}\text{Nd}$  (4.1),  $^{145}\text{Nd}$  (231), and  $^{146}\text{Nd}$  (2.7 barns). These values are used in the calculations presented here. In contrast, Nyquist et al. (1995) and Boyet and Carlson (2007) used  $^{149}\text{Sm}$   $\sigma_{\text{eff}}$  ranging from 41,000 to 56,000 barns. These values are not based on the most recent data available in the published nuclear data.

Because the calculated thermal neutron flux is inversely proportional to the measured  $\epsilon^{149}\text{Sm}$ , using smaller  $^{149}\text{Sm}$   $\sigma_{\text{eff}}$  values results in larger corrections to Nd isotopes (Fig. 2, Table 5). Whether the corrections using the smaller  $^{149}\text{Sm}$   $\sigma_{\text{eff}}$  values are realistic can be evaluated using the corrections to  $^{145}\text{Nd}$  as noted above. The higher calculated  $\Psi$  also means a proportionally higher  $\Xi$  when the  $\Psi/\Xi$  remains the same. In Table 5 and Fig. 3, four different neutron fluence models are considered for calculating  $\mu^{145}\text{Nd}$ . Model 1 in Fig. 3A, follows Rankenburg et al. (2006) to calculate the corrected  $\mu^{145}\text{Nd}$  for each sample using a  $^{149}\text{Sm}$   $\sigma_{\text{eff}}$  to be 71,267 barns and a  $\Psi/\Xi$  of 1.1, where the latter is identical to the direct measurements of Apollo 17 samples in the LNPE experiment. For the samples in this study, all of the corrected  $\mu^{145}\text{Nd}$  fall within the external precision range of  $\pm 4.1$  ppm ( $2\sigma$ ) of the terrestrial standard (Fig. 3A, Table 5) and give an average of  $1 \pm 2.7$  ( $2\sigma$ ). For the static and multidynamic measurements of Boyet and Carlson (2007), the corrected  $\mu^{145}\text{Nd}$  fall within a  $\pm 10$  ppm range of the terrestrial standard with the exception of 12016, where the measured  $\mu^{145}\text{Nd}$  has a large uncertainty of  $\pm 12.2$  ppm ( $2\sigma$ ). In particular, the three multidynamic measurements of Boyet and Carlson (2007), all have corrected  $\mu^{145}\text{Nd}$  to  $\pm 5$  ppm of the terrestrial standard. Three other models are presented in Fig. 3B and Table 5. Model 2 uses a  $\Psi/\Xi = 0.5$  with  $^{149}\text{Sm}$   $\sigma_{\text{eff}}$  71,627

Table 5

Neutron Fluence corrections to Nd isotopes. Samples from the present study and those from Boyet and Carlson (2007) are listed with the latter being designated ‘BC’ prior to the sample designation. Samples from Boyet and Carlson (2007) measured in multidynamic mode are designated with a ‘M’ following the sample designation. The  $\mu^{145}\text{Nd}$  for all BC samples including those run for multidynamic  $^{142}\text{Nd}/^{144}\text{Nd}$ , were measured in static mode, and these unpublished data are used with permission (R.W. Carlson, pers. comm. 2009). The effective thermal neutron flux ( $\Psi$ , in  $\text{n}/\text{cm}^2$ ) and neutron corrected  $\mu^{142}\text{Nd}$  and  $\mu^{145}\text{Nd}$  for 4 different models using the measured  $\varepsilon^{149}\text{Sm}$  of each sample in Equation (2) of Nyquist et al. (1995), and for the following: (1)  $^{149}\text{Sm}$   $\sigma_{\text{eff}} = 71,627$  barns ( $10^{-24} \text{ cm}^2$ ),  $\Psi/\theta = 1.1$ ; (2)  $^{149}\text{Sm}$   $\sigma_{\text{eff}} = 71,627$  barns,  $\Psi/\theta = 0.5$ ; (3)  $^{149}\text{Sm}$   $\sigma_{\text{eff}} = 56,000$  barns ( $10^{-24} \text{ cm}^2$ ),  $\Psi/\theta = 1.1$ ; (4)  $^{149}\text{Sm}$   $\sigma = 41,800$  barns ( $10^{-24} \text{ cm}^2$ ),  $\Psi/\theta = 1.1$ . Correction of  $^{142}\text{Nd}$  produced from  $^{141}\text{Pr}$  was made in each sample using the measured Pr/Nd compiled in the Apollo Lunar Sample Compendium (Meyer, 2009). Details of the models are discussed in the text.

Sample	$\mu^{142}\text{Nd}$	$\pm 2\sigma$	$\mu^{145}\text{Nd}$	$\pm 2\sigma$	$\varepsilon^{149}\text{Sm}$	1 $\Psi$ $\text{n}/\text{cm}^2$	1 $\mu^{142}\text{Nd}$ corr	1 $\mu^{145}\text{Nd}$ corr	2 $\mu^{142}\text{Nd}$ corr	2 $\mu^{145}\text{Nd}$ corr	3 $\Psi$ $\text{n}/\text{cm}^2$	3 $\mu^{142}\text{Nd}$ corr	3 $\mu^{145}\text{Nd}$ corr	4 $\Psi$ $\text{n}/\text{cm}^2$	4 $\mu^{142}\text{Nd}$ corr	4 $\mu^{145}\text{Nd}$ corr
SAU 169	-26.3	2.4	-7.2	2.9	-12.4	1.724E+16	-20.5	-0.3	-20.3	5.5	2.205E+16	-18.9	1.7	2.955E+16	-16.3	4.7
15386	-31.1	1.6	-14.9	4.0	-32.2	4.496E+16	-15.9	3.2	-15.6	18.2	5.750E+16	-11.7	8.2	7.703E+16	-5.1	16.1
LAP 02205	-8.4	0.8	0.0	2.5	-3.7	5.166E+15	-6.6	2.1	-6.6	3.8	6.607E+15	-6.2	2.7	8.852E+15	-5.4	3.6
15555	-5.9	6.2	-2.3	1.9	-5.7	7.958E+15	-3.2	0.9	-3.1	3.6	1.018E+16	-2.4	1.8	1.364E+16	-1.3	3.2
70017	13.4	0.9	-1.0	3.4	-2.0	2.792E+15	14.4	0.1	14.4	1.1	3.571E+15	14.6	0.4	4.785E+15	15.1	0.9
74275	16.2	1.8	-0.8	3.4	-1.8	2.513E+15	17.1	0.2	17.1	1.0	3.214E+15	17.3	0.5	4.306E+15	17.7	0.9
BC12016	5.0	16.0	8.0	12.2	-7.3	1.019E+16	8.4	12.1	8.5	15.5	1.304E+16	9.4	13.2	1.746E+16	10.9	15.0
BC12038	-26.0	7.0	-17.0	5.7	-27.1	3.783E+16	-13.1	-1.8	-12.7	10.8	4.839E+16	-9.6	2.5	6.483E+16	-4.0	9.1
BC12039	-14.0	4.0	-27.0	3.1	-42.6	5.947E+16	6.2	-3.1	7.0	16.8	7.607E+16	11.9	3.6	1.019E+17	20.7	14.0
BC15555	-2.0	6.0	-4.0	4.6	-6.2	8.656E+15	0.9	-0.5	1.0	2.4	1.107E+16	1.8	0.5	1.483E+16	3.0	2.0
BC15555M	-10.0	4.0	2.0	1.7	-5.6	7.818E+15	-7.3	5.1	-7.2	7.8	1.000E+16	-6.6	6.0	1.340E+16	-5.4	7.4
BC10003	15.0	4.0	-5.0	3.7	-3.0	4.188E+15	16.4	-3.3	16.5	-1.9	5.357E+15	16.8	-2.8	7.177E+15	17.4	-2.1
BC10072	5.0	5.0	-17.0	3.8	-11.8	1.647E+16	10.6	-10.4	10.8	-4.9	2.107E+16	12.2	-8.5	2.823E+16	14.6	-5.6
BC70017	13.0	5.0	1.0	3.8	-1.7	2.373E+15	13.8	2.0	13.9	2.7	3.036E+15	14.0	2.2	4.067E+15	14.4	2.6
BC70017M	11.0	5.0	3.0	1.7	-1.7	2.373E+15	11.8	4.0	11.9	4.7	3.036E+15	12.0	4.2	4.067E+15	12.4	4.6
BC75075	25.0	9.0	2.0	7.1	-4.6	6.422E+15	27.2	4.6	27.3	6.7	8.214E+15	27.8	5.3	1.100E+16	28.8	6.4
BC14310	-20.0	5.0	-6.0	3.6	-24.9	3.476E+16	-8.3	8.0	-7.9	19.6	4.446E+16	-5.0	11.9	5.957E+16	0.1	18.0
BC14310M	-32.0	5.0	-15.0	2.4	-24.1	3.365E+16	-20.6	-1.5	-20.3	9.8	4.304E+16	-17.5	2.3	5.766E+16	-12.5	8.2
BC60025	-21.0	5.0	6.0	5.5	-0.4	5.584E+14	-20.8	6.2	-20.8	6.4	7.143E+14	-20.8	6.3	9.569E+14	-20.7	6.4
BC78236	-19.0	4.0	-10.0	3.4	-29.0	4.049E+16	-5.4	6.3	-5.0	19.8	5.179E+16	-1.6	10.8	6.938E+16	4.3	17.9

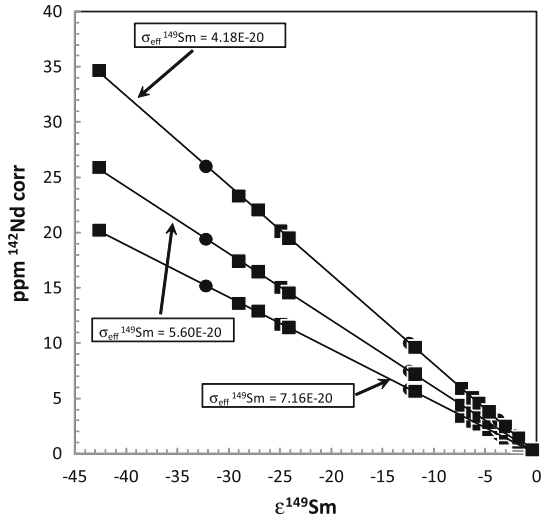


Fig. 2. The measured  $\epsilon^{149}\text{Sm}$  measured versus the ppm correction to  $^{142}\text{Nd}/^{144}\text{Nd}$  (ppm  $^{142}\text{Nd}$  corr) for the averaged multidynamic data in this study (solid circles), and all samples from Boyett and Carlson (2007) (solid squares) are plotted for neutron fluence correction Models 1, 3, and 4 in Table 5, having  $\sigma_{\text{eff}}^{149}\text{Sm}$  of 71,627, 56,000, and 41,800 barns, respectively (Nyquist et al., 1995; Rankenburg et al. 2006; Boyett and Carlson, 2007). See Table 5 and the text for details.

barns, whereas Models 3 and 4, use the lower  $^{149}\text{Sm}$   $\sigma_{\text{eff}}$  values of 56,000 and 41,800 barns and a  $\Psi/\Xi = 1.1$  used in the Rankenburg et al. (2006) model, respectively. In all cases, these models have greater  $\Xi$  as a result of either higher  $\Psi$  in Models 3 and 4, and a lower  $\Psi/\Xi$  in Model 2. For the samples from both studies with the lowest  $\epsilon^{149}\text{Sm}$  and thus the largest amount of exposure to neutron fluence, the corrected values for  $\mu^{145}\text{Nd}$  are collectively higher than they should be (Fig. 3B). In Models 3 and 4 using the older, and lower values for  $^{149}\text{Sm}$   $\sigma_{\text{eff}}$ , the only way to alleviate this problem is to significantly lower  $\Xi$  applied in the calculations. For example, applying  $\Psi/\Xi$  of 2 and 3 for Models 3 and 4, respectively, can erase the over-correction to  $\mu^{145}\text{Nd}$  of sample 15386 of this study, and can mostly erase the over-correction to  $\mu^{145}\text{Nd}$  in samples analyzed by Boyett and Carlson (2007) study. However, this does not reduce the increased scatter in corrected  $\mu^{142}\text{Nd}$  between the 3 KREEP samples measured multidynamically when applying Models 3 and 4 as noted in the following paragraph. Nevertheless, it remains for additional studies to determine whether  $\Psi/\Xi$  higher than the 1.1 obtained in the LPNE study are relevant for correcting lunar mare basalts for neutron fluence.

The samples from Rankenburg et al. (2006), Boyett and Carlson (2007) and this study with the preferred Model 1 correction in Table 5 are plotted for corrected  $\mu^{142}\text{Nd}$  versus the measured  $^{147}\text{Sm}/^{144}\text{Nd}$  in Fig. 4. The six samples from this study and the three samples measured multidynamically from Boyett and Carlson (2007), all plot on a trend that is intermediate to the trends for the static measurements from the two previous studies. The correlation of this trend for the six samples from this study has  $R^2 = 0.97$ . This trend for the multidynamic data from the

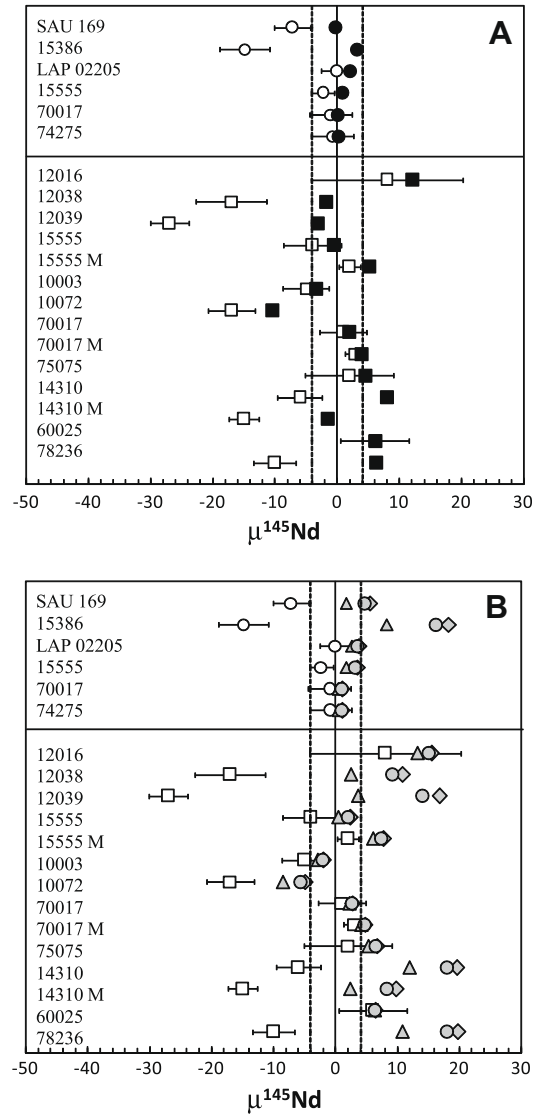


Fig. 3. (A) The measured  $\mu^{145}\text{Nd}$  (open symbols) and neutron fluence corrected  $\mu^{145}\text{Nd}$  using Model 1 in Table 5 (solid symbols), for the averaged multidynamic data in this study (circles) and all samples (squares) from Boyett and Carlson (2007). The latter are unpublished data from the same runs for  $^{142}\text{Nd}/^{144}\text{Nd}$  presented in Boyett and Carlson (2007) and used with permission (R.W. Carlson, pers. comm. 2009). The  $\mu^{145}\text{Nd}$  data measured statically for the samples measured multidynamically for  $^{142}\text{Nd}/^{144}\text{Nd}$  by Boyett and Carlson (2007) have an ‘M’ following the sample number, whereas samples with no designation are from static  $^{142}\text{Nd}/^{144}\text{Nd}$  measurements. Error bars are  $2\sigma$ . (B) The same samples listed as in (A), but the neutron fluence corrected  $\mu^{145}\text{Nd}$  values were obtained using Model 2 (shaded diamonds), Model 3 (shaded triangles), and Model 4 (shaded circles) in Table 5. Error bars are  $2\sigma$ .

two studies has more scatter if the corrected range of  $\mu^{142}\text{Nd}$  values using the neutron fluence Models 3 and 4 are used instead of the preferred Model 1. This is primarily because KREEP basalt 15386 measured in this study has received a greater amount of neutron fluence than KREEP impact melts SAU 169, and 14310 measured by Boyett and Carlson (2007). Using Model 1, these 3 KREEP

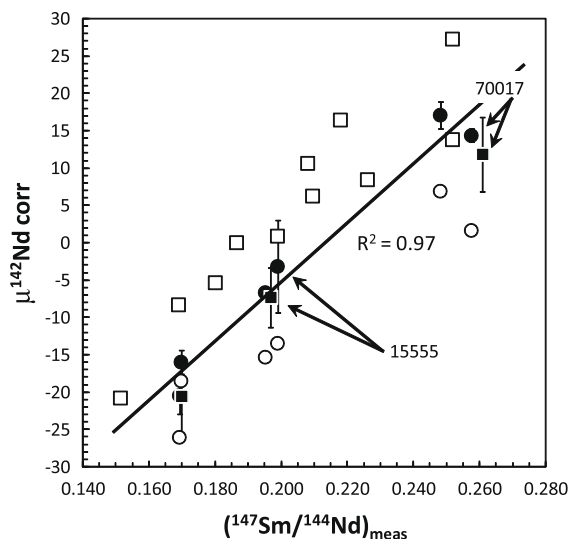


Fig. 4. The  $(^{147}\text{Sm}/^{144}\text{Nd})_{\text{meas}}$  (measured) versus  $\mu^{145}\text{Nd}$  corr (neutron fluence corrected) using Model 1 of Table 5 for multidynamic data in this study (solid circles), static data (open circles) from Rankenburg et al. (2006), multidynamic data (solid squares) and static data (open squares) from Boyet and Carlson (2007). Error bars are  $2\sigma$  and only shown for the multidynamic data from the two labs. A regression line with  $R^2 = 0.97$  is shown for the data from this study. Error bars for the static data are typically larger and are not shown for clarity.

samples measured multidynamically in this study and Boyet and Carlson (2007) with similar  $^{147}\text{Sm}/^{144}\text{Nd}$  ratios form a tight cluster in Fig. 4 with a range of corrected  $\mu^{142}\text{Nd}$  of  $-15.9$  to  $-20.6$  (4.7 ppm range). Applying Models 3 and 4 to these data results in significant increases in the ranges of corrected  $\mu^{142}\text{Nd}$ , from  $-11.7$  to  $-18.9$  (7.2 ppm range), and  $-5.1$  to  $-16.3$  (10.2 ppm range), respectively (Table 5). Without any assumptions yet applied to the source  $^{147}\text{Sm}/^{144}\text{Nd}$  for these samples, these relationships show that the neutron fluence Model 1 for Nd isotope correction of multidynamic analysis from two separate studies produces the best correlation and independently verifies the relationships for correcting  $\mu^{145}\text{Nd}$  discussed above. In conjunction with the conclusions from the previous section on reproducibility of static versus multidynamic data for the lunar mare basalts, from hereon only the multidynamic data, using the Model 1 neutron fluence corrections, are considered for the models of the Sm–Nd relationships of the Moon.

### 5. COUPLED $^{142}\text{Nd}$ – $^{143}\text{Nd}$ MODELS FOR EARLY LUNAR EVOLUTION

Coupled  $^{142}\text{Nd}$ – $^{143}\text{Nd}$  isotope systematics have been employed to constrain differentiation timescales of terrestrial bodies in the first several hundred million years of the solar system history (e.g. Nyquist et al., 1995; Harper et al., 1995; Caro et al., 2003; Foley et al., 2005; Boyet and Carlson, 2005; Andreasen and Sharma, 2006; Caro et al., 2006; Rankenburg et al., 2006; Debaille et al., 2007; Bennett et al., 2007; Boyet and Carlson, 2007; Andreasen et al., 2008; Caro et al., 2008). For lunar samples, the three previ-

ous studies (Nyquist et al., 1995; Rankenburg et al., 2006; Boyet and Carlson, 2007) used the Sm–Nd isotope systematics measured to calculate the source  $^{147}\text{Sm}/^{144}\text{Nd}$  ratio for each sample and plot these values against  $^{142}\text{Nd}/^{144}\text{Nd}$  ratios. As in the relationship between measured  $^{147}\text{Sm}/^{144}\text{Nd}$  versus  $\mu^{142}\text{Nd}$  (Fig. 4), well-defined positive correlations between them are observed. In each case and depending on the absolute values of  $^{142}\text{Nd}/^{144}\text{Nd}$  ratios and the assumptions on calculating source  $^{147}\text{Sm}/^{144}\text{Nd}$  ratios, the positive correlation provides an isochron age ranging from around 200–250 Ma after the onset of nebular condensation (ONC) at 4.569 Ga (Bouvier et al., 2007). Where the  $^{142}\text{Nd}$ -source versus source  $^{147}\text{Sm}/^{144}\text{Nd}$  correlation intersects the 4.569 Ga chondrite isochron for the static data of Rankenburg et al. (2006), an initial value of  $\mu^{142}\text{Nd} = -18.9 \pm 2.2$  ( $2\sigma$ ) and an apparent lunar isochron age of  $215^{+23}_{-21}$  Ma<sub>ONC</sub> are derived. The calculated  $\mu^{142}\text{Nd}$  of  $-18.9 \pm 2.2$  is within error of the present-day average value for chondrites of  $\sim -20$  (Bouvier and Carlson, 2005; Andreasen and Sharma, 2006; Carlson et al., 2007). Rankenburg et al. (2006) thus concluded that the Moon has a chondritic bulk Sm/Nd ratio and that the source regions for the lunar mare basalts all closed with respect to the Sm–Nd system at 215 Ma<sub>ONC</sub>. In contrast, because the static data of Boyet and Carlson (2007) plot at 10–20 ppm higher for  $\mu^{142}\text{Nd}$  for a given sample or petrologic type than do the Rankenburg et al. (2006) data (Fig. 4), these authors argued that the Moon has a bulk Sm/Nd ratio that was larger than chondritic and similar to the Earth's present-day convecting mantle. The isochron determined by Boyet and Carlson (2005) has a comparable slope to that of Rankenburg et al. (2006), although with more scatter, and defines an age range between  $\sim 210$  and 255 Ma<sub>ONC</sub> depending on assumed initial Sm/Nd ratios and whether 1 or two stages of differentiation occurred.

Following the methods developed by these workers we report on three different models that we use to evaluate the multidynamic  $\mu^{142}\text{Nd}$  data of this study. The absolute age information obtained from these models depends on the model parameters, and each age quoted below can be adjusted using different constants. What is important is the relative timing calculated between the different basalt groups representing different lunar mantle sources, and where they plot relative to each other in terms of their  $^{142}\text{Nd}/^{144}\text{Nd}$  and  $^{143}\text{Nd}/^{144}\text{Nd}$  isotope systematics. In each of the models, the solar system initial  $^{146}\text{Sm}/^{144}\text{Sm}$  ratio used at 4.569 Ga is 0.008 and based on determinations by Lugmair and Galer (1992), Nyquist et al. (1994), Amelin and Rotenberg (2004), and references therein. The most precise estimation of solar system initial  $^{146}\text{Sm}/^{144}\text{Sm}$  ratio is  $0.0080 \pm 0.0009$  ( $2\sigma$ ) obtained at 4.569 Ga from  $0.0076 \pm 0.0009$  at 4.558 Ga for the angrite LEW 86010 (Nyquist et al., 1994). Varying this ratio by 20% (i.e. 0.0064–0.0096) does not affect the interpretations of the systematics discussed for each model below. The relative timing between the different basalt groups calculated source reservoirs remains the same in Models A and B, and in the multistage Model C, the age obtained for the lunar isochron is within error of that calculated using  $^{146}\text{Sm}/^{144}\text{Sm} = 0.008$ .

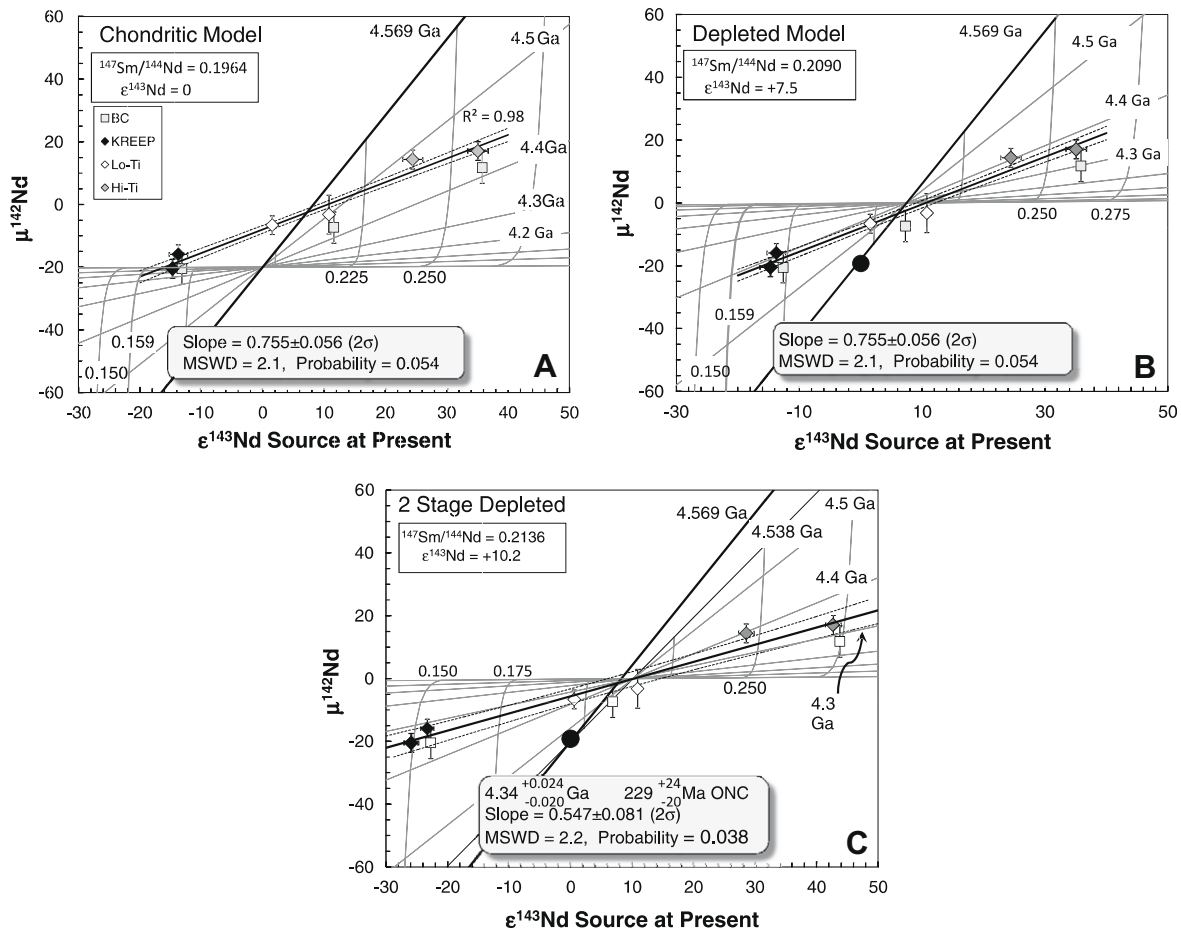


Fig. 5. Coupled  $\mu^{142}\text{Nd}$ – $\epsilon^{143}\text{Nd}$  source models. The calculated source compositions for the data from this study and the multidynamic data (BC, squares) from (Boyet and Carlson, 2007) are plotted. The  $\mu^{142}\text{Nd}$  error bars are  $\pm 3$  ppm for the data in this study, based on long-term external reproducibility of the standard for the JSC Triton from 2007 to 2009, with the exception of sample 15555, where the error of the average in Table 3 is used. The error for calculated  $\epsilon^{143}\text{Nd}$  of the source for each sample in this study takes into account the  $\pm 0.2\%$  uncertainty in the Sm/Nd obtained from isotope dilution measurements and the Sm–Nd mixed spike uncertainties. The error bars for the  $\mu^{142}\text{Nd}$  data from Boyet and Carlson are their reported  $\pm 2\sigma$  for each sample. Sources were evolved to the present-day so that the sources derived for samples with different crystallization ages can be compared directly. Crystallization ages for the samples in this study are from Rankenburg et al. (2006), Rankenburg et al. (2007), and references therein and listed in Table 1. Crystallization ages for the samples from Boyet and Carlson (2007) are listed in that paper. No corrections were applied to the measured  $\mu^{142}\text{Nd}$  to obtain source  $\mu^{142}\text{Nd}$  at present. This is because the combined correction to initial  $\mu^{142}\text{Nd}$  at the time of crystallization followed by recalculating the present-day  $\mu^{142}\text{Nd}$  of the source based on the calculated source  $^{147}\text{Sm}/^{144}\text{Nd}$  of each sample effectively cancels out as each is less than 1 ppm in difference to the present-day measured  $\mu^{142}\text{Nd}$ . This is a result of the fact that  $^{146}\text{Sm}$  is more than 99.99% decayed away by the time of crystallization of even the oldest of the mare basalt samples in this study. A regression line with  $\pm 2\sigma$  error envelopes (dashed lines) through the sources calculated from the data in this study using IsoPlot (Ludwig, 2003) with an  $R^2 = 0.98$  is shown in each diagram. The lines for constant source  $^{147}\text{Sm}/^{144}\text{Nd}$  are shown in the diagram for increments of 0.025, and isochrons for differentiation times are shown for 100 Ma intervals. The 4.569 solar system isochron is shown, and all models are developed using a present-day chondrite average of  $\mu^{142}\text{Nd} = -20$ ,  $\epsilon^{143}\text{Nd} = 0$ ,  $^{147}\text{Sm}/^{144}\text{Nd} = 0.1964$ , and an initial solar system  $^{146}\text{Sm}/^{144}\text{Sm} = 0.008$  at 4.569 Ga. Equations adapted for the calculations have been published elsewhere (Rankenburg et al., 2006; Bennett et al., 2007; Debaille et al., 2007). (A) A chondritic model for the bulk material that makes up the Moon. (B) A depleted model that evolves to present-day  $\epsilon^{143}\text{Nd} = +7.5$  with a material having  $^{147}\text{Sm}/^{144}\text{Nd} = 0.2090$  at or near the onset of nebular condensation at 4.569 Ga. Regression of the data is identical to that for (A). (C) A two-stage differentiation model for the Moon. In the first stage, fractionation between Sm and Nd for the material that makes up the Moon leads to a  $^{147}\text{Sm}/^{144}\text{Nd} = 0.2136$  at 4.538 Ga, or 31 Ma after the onset of nebular condensation (ONC) and prior to lunar formation at  $\sim 60$  to 110 Ma<sub>ONC</sub>. The Moon then undergoes large-scale differentiation to create the source regions of KREEP, Lo–Ti, and Hi–Ti sources at  $4.340^{+0.024}_{-0.020}$  Ga, or  $229^{+24}_{-20}$  Ma<sub>ONC</sub>. The  $\pm 2\sigma$  error for the isochron age is based on the error calculated for the regression using IsoPlot.

In first model, it is assumed that the Moon has a chondritic bulk  $^{147}\text{Sm}/^{144}\text{Nd} = 0.1964$ , and there was one stage of differentiation for each calculated source  $^{147}\text{Sm}/^{144}\text{Nd}$  ratio for each sample prior to the time of magma generation. In a second model, it is assumed that the Moon has

a bulk  $^{147}\text{Sm}/^{144}\text{Nd} = 0.209$ , required to give a present-day  $\mu^{142}\text{Nd} = 0$  and identical to the terrestrial standard in a 1 stage differentiation model similar to the first model. Finally, in a third model it is assumed that the Moon has a bulk  $^{147}\text{Sm}/^{144}\text{Nd}$  of 0.2136 and has a linked two-stage

differentiation for all of the samples. The reason for the more complex third model is discussed below.

The models and calculated sources for mare basalt data are shown in present-day  $\epsilon^{143}\text{Nd}-\mu^{142}\text{Nd}$  isochron diagrams (Fig. 5), where  $\epsilon^{143}\text{Nd}$  for the source at present is calculated from the initial  $\epsilon^{143}\text{Nd}$  at the time of crystallization and evolved to the present using the calculated source  $^{147}\text{Sm}/^{144}\text{Nd}$  ratio of each sample. This is done so that the Sm–Nd relationships for each sample that crystallized at times from 3.90 Ga to 2.99 Ga can be compared directly. For the chondritic model (Fig. 5A), the calculated points for the 6 samples in this study plot on a well-defined correlation line with an  $R^2 = 0.98$ , based on regression of the data using IsoPlot (Ludwig, 2003). The three multidynamic data of Boyet and Carlson (2007) plot at 0.1–4.6 ppm less for correlative KREEP, Lo–Ti, and Hi–Ti samples in this study, but overlap within uncertainty. The correlation does not pass through the origin point and is consequently not isochronous. The source for Hi–Ti would have a Sm–Nd differentiation age of  $\sim 4.43$  Ga, for the Lo–Ti,  $\sim 4.5$  Ga, and for KREEP, as young as 4 Ga. The KREEP source likely represents quenched residual liquid from a lunar magma ocean (Snyder et al., 1992). The KREEP source can be as old as 4.2–4.25 Ga in this model of it is has a  $^{147}\text{Sm}/^{144}\text{Nd}$  of 0.159–0.150 (Fig. 5A). A lower source  $^{147}\text{Sm}/^{144}\text{Nd}$  ratio than  $\sim 0.150$  for residual liquids of magma ocean crystallization, is inconsistent with known partitioning behavior of Sm and Nd (Debaille et al., 2008). Such a young age for the KREEP source is inconsistent with the age derived by other isotopic systems. The  $^{87}\text{Rb}-^{87}\text{Sr}$ ,  $^{238,235}\text{U}-^{206,207}\text{Pb}$ , and  $^{147}\text{Sm}-^{143}\text{Nd}$  model ages for the KREEP source are older and range from  $4.36 \pm 0.06$  to  $4.42 \pm 0.07$  Ga (Tera and Wasserburg, 1974; Carlson and Lugmair 1979; Nyquist and Shih, 1992; Boyet and Carlson, 2007). In this model, the calculated sources for the three mare basalt types formed at different times but lie on a well-defined correlation line. Such a

coincidence is unlikely, and in combination with this model giving an unsupported young age for KREEP and a  $\geq 4.5$  Ga age for the source of Lo–Ti basalts, a scenario where the Moon has a bulk Sm/Nd similar to average chondrites is unlikely. An alternative would be that the trend represents a mixing line between KREEP and Hi–Ti sources or melts. This possible scenario is considered in Section 6.

For a depleted model where the Moon has a bulk  $^{147}\text{Sm}/^{144}\text{Nd} = 0.209$ , there is also an identical well-defined correlation similar to that of the chondritic model between the data points for  $\mu^{142}\text{Nd}$  versus  $\times$  present-day source  $\epsilon^{143}\text{Nd}$  (Fig. 5B). The line nearly intersects the 4.569 Ga isochron at the value of  $\mu^{142}\text{Nd} = 0$ , and therefore is internally consistent with a depleted bulk Sm/Nd ratio for the Moon. Taking the formation ages at face value, the Hi–Ti source formed at 4.4–4.35 Ga, whereas the KREEP source formed earlier at  $\geq 4.4$  Ga. In this model, the well-defined trend between the calculated source compositions for KREEP, Lo–Ti, and Hi–Ti samples is a mixing line between KREEP and Hi–Ti end-members. In this scenario, the Lo–Ti samples are mixtures between KREEP-rich melts and Hi–Ti melts, or is a hybrid source intermediate between the two. This scenario is tested further in Section 6.

A more complex two-stage differentiation model, where the sources for KREEP, Lo–Ti, and Hi–Ti samples formed near contemporaneous from a Moon with a depleted Sm/Nd ratio relative to that of chondrites, is evaluated in Fig. 5C. In this case, the Moon formed from material that had a  $^{147}\text{Sm}/^{144}\text{Nd} = 0.2136$ , similar to the present-day MORB reservoir in Earth (Jacobsen, 1988; Salters and Stracke, 2004) at 4.538 Ga. The model begins with a  $^{146}\text{Sm}/^{144}\text{Sm} = 0.008$  and  $^{147}\text{Sm}/^{144}\text{Nd} = 0.1964$  at 4.569 Ga (the value for an initial for the bulk solar system with average chondritic values, Table 6) followed by fractionation of Sm/Nd at 4.538 Ga (31  $\text{Ma}_{\text{ONC}}$ ) to a depleted  $^{147}\text{Sm}/^{144}\text{Nd} = 0.2136$  and  $^{146}\text{Sm}/^{144}\text{Sm} = 0.00649$ . This is

Table 6

The  $^{146}\text{Sm}/^{144}\text{Sm}$  and  $^{147}\text{Sm}/^{144}\text{Nd}$  parameters used for coupled  $^{142}\text{Nd}-^{143}\text{Nd}$  models. The model numbers (A), (B), and (C) correspond to the models presented in Fig. 5A–C, respectively. For model (C) the source  $^{147}\text{Sm}/^{144}\text{Nd}$  ratios for the samples are calculated at 4.329 Ga the time of second-stage differentiation of the lunar mantle, while the source  $^{147}\text{Sm}/^{144}\text{Nd}$  ratios for models (A) and (B) are calculated for a one-stage evolution. Equations used in the calculations are from Rankenburg et al. (2006) and references therein. The initial source parameter for chondritic (A) and depleted (B) are for single stage evolution from 4.569 Ga, while the two-stage depleted (C) is for a chondritic starting source at 4.569 Ga with Sm/Nd fractionation at 4.538 Ga to a depleted composition as listed. Additional model parameters and explanations are in Fig. 5 and the text.

Sample	Type	$^{147}\text{Sm}/^{144}\text{Nd}$ Source chondritic (A)	$^{147}\text{Sm}/^{144}\text{Nd}$ Source depleted (B)	$^{147}\text{Sm}/^{144}\text{Nd}$ Source two-stage depleted (C)
SAU169 1-1	KREEP	0.1717	0.1717	0.1495
SAU169 1-2	KREEP	0.1715	0.1715	0.1492
15386 1-1	KREEP	0.1732	0.1732	0.1540
LAP 02205 1-1	Low-Ti	0.1190	0.1190	0.1965
15555 1-1	Low-Ti	0.2145	0.2145	0.2149
70017 1-1	High-Ti	0.2377	0.2377	0.2464
74275 1-1	High-Ti	0.2558	0.2558	0.2716
74275 1-2	High-Ti	0.2556	0.2556	0.2714
Initial source parameters	$^{146}\text{Sm}/^{144}\text{Sm}$ 4.569 Ga	$^{147}\text{Sm}/^{144}\text{Nd}$ 4.569 Ga	$^{146}\text{Sm}/^{144}\text{Sm}$ 4.538 Ga	$^{147}\text{Sm}/^{144}\text{Nd}$ 4.538 Ga
Chondritic (A)	0.00800	0.1964	–	–
Depleted (B)	0.00800	0.2090	–	–
Two-stage depleted (C)	0.00800	0.1964	0.00649	0.2136

only solution where there is an internally consistent model – where the terrestrial standard with  $\mu^{142}\text{Nd} = 0$  intersects the regression line for the new lunar basalt data (Fig. 5C), and the present-day chondrite average  $\mu^{142}\text{Nd} = -20$ . In such a case, the new lunar basalt data regression line corresponds to an isochron in the differentiation model (Fig. 5C). If the time of Sm/Nd fractionation is  $46 \text{ Ma}_{\text{ONC}}$ , the  $^{147}\text{Sm}/^{144}\text{Nd} = 0.2154$  and corresponding  $^{146}\text{Sm}/^{144}\text{Sm} = 0.005867$  at that time to generate a present-day difference between chondrites and the terrestrial standard of 20 ppm. For a time of Sm/Nd fractionation of  $16 \text{ Ma}_{\text{ONC}}$ , the  $^{147}\text{Sm}/^{144}\text{Nd} = 0.2119$  and corresponding  $^{146}\text{Sm}/^{144}\text{Sm} = 0.007182$  at that time to generate a present-day difference between chondrites and the terrestrial standard of 20 ppm. These two examples do not exactly intersect the regression line for the lunar basalt data at  $\mu^{142}\text{Nd} = 0$  and no isochron can be calculated (Fig. 5C). In this model, the well-defined correlation for the present-day calculated sources of the different lunar mare basalt samples plot as an isochron with an age of  $4.340^{+0.024}_{-0.020} \text{ Ga}$ , or  $229^{+24}_{-20} \text{ Ma}_{\text{ONC}}$ . This is consistent with a 44 Ma or smaller formation interval for these different reservoirs. The implications from the results of this model are evaluated below.

## 6. Nd–Hf ISOTOPE RELATIONSHIPS IN THE EARLY MOON

The models in the previous section indicate that a bulk Moon having a chondritic Sm/Nd ratio is inconsistent with the coupled  $\mu^{142}\text{Nd}$ – $\epsilon^{143}\text{Nd}$  systematics of the calculated sources of the lunar mare basalts unless a mixing relationship exists between KREEP, Lo–Ti, and Hi–Ti sources or melts, and the age of the KREEP source is 4.25 Ga or younger, an unlikely scenario. Instead, models for a Moon having a superchondritic Sm/Nd broadly similar to that of the Earth’s present-day convecting mantle and/or the source of depleted MORB, are most consistent with the new Nd isotope results presented here. These conclusions are consistent with those drawn by Boyet and Carlson (2007), and allow the use of the new and possibly more accurate multidynamic Nd isotoped data in this present study and those from Boyet and Carlson (2007) to further examine the implications for early differentiation of the Moon. The well-correlated  $^{142}\text{Nd}$ – $^{143}\text{Nd}$  data in Fig. 5B and C can be interpreted to result from two-component mixing of melts with source regions formed at variable times in the early Moon, or may result from formation of the sources of KREEP, Lo–Ti, and Hi–Ti mare basalts formed within an interval  $229^{+24}_{-20} \text{ Ma}_{\text{ONC}}$ , and do not require mixing between two components to generate the well-correlated trends.

Mixing relationships between mare basalt source regions can be well constrained by Nd and Hf isotope systematics (Beard et al., 1998) and we examine these possibilities below. The six samples from this study were measured for Lu–Hf isotopes on the same sample aliquots as those used for the high-precision Nd isotope ratio measurements (Table 1). Using these new Hf isotope data and those in the literature (Unruh et al., 1984; Beard et al., 1998), the  $\epsilon^{176}\text{Hf}$  ( $10^4$  parts variation relative to CHUR, Bouvier et al., 2008) for the sources of these mare basalts evolved to the present are calculated and combined with those for

$\epsilon^{143}\text{Nd}$  of the sources at present. The isotope relationships presented in Fig. 6 were calculated using the assumption of a starting lunar mantle having present-day average depleted MORB  $^{176}\text{Lu}/^{177}\text{Hf} = 0.0389$  and  $^{147}\text{Sm}/^{144}\text{Nd} = 0.2136$ , with a fractionation event at 4.34 Ga to derive the lunar source reservoirs following the calculations for data presented in Fig. 5C. Using a chondritic or depleted starting Moon with a single fractionation event does not change the systematic differences between data plotted in Fig. 6, but instead shifts all the points in the same manner by a few epsilon units. These data show that the lunar interior at present must have a much greater isotopic diversity than the Earth’s modern oceanic mantle (Fig. 6). The calculated sources for all lunar basalts appear to fall between three hypothetical end-members – KREEP source, ILM source (Apollo 12 ilmenite mare basalt), and Hi–Ti source (Apollo 11 and 17 Hi–Ti mare basalt). Three hypothetical mixing lines may explain the isotope diversity observed – ILM  $\leftrightarrow$  KREEP, Hi–Ti  $\leftrightarrow$  KREEP with hyperbolic curve through Lo–Ti source, and Hi–Ti  $\leftrightarrow$  KREEP with a linear mixing line. Out of these three only the hyperbolic curve can explain the Lo–Ti source as a mixture between KREEP and Hi–Ti, as required by the coupled relationships between  $\mu^{142}\text{Nd}$  and  $\epsilon^{143}\text{Nd}$  (Fig. 5).

To evaluate the possible mixing between KREEP and Hi–Ti sources or melts to derive the Lo–Ti Hf–Nd isotope

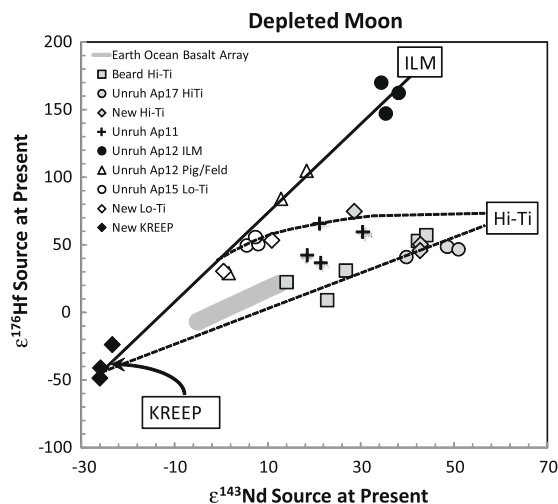


Fig. 6. Coupled  $\epsilon^{143}\text{Nd}$ – $\epsilon^{176}\text{Hf}$  source models. The depleted model described in the text and plotted in Fig. 5C was used for Nd isotopes, and correlative Lu–Hf calculations were performed and evolved to the present-day with the following parameters:  $\lambda^{176}\text{Lu} = 1.867 \text{ E-11}$ , Present-day  $^{176}\text{Hf}/^{177}\text{Hf}_{\text{CHUR}} = 0.282785$ ,  $^{176}\text{Lu}/^{177}\text{Hf}_{\text{CHUR}} = 0.0336$ ,  $^{176}\text{Hf}/^{177}\text{Hf}_{\text{MORB}} = 0.283279$ ,  $\epsilon^{176}\text{Hf}_{\text{MORB}} = +17.5$ , and  $^{176}\text{Lu}/^{177}\text{Hf}_{\text{MORB}} = 0.03915$  (Bouvier et al., 2008; Chauvel et al., 2008). The field for the Earth Ocean Basalt Array is from the compiled data in Chauvel et al. (2008). The calculated sources for the Beard Hi–Ti uses Lu–Hf isotope data from Beard et al. (1998) from Apollo 11 and 17 Hi–Ti mare basalt samples, and Sm–Nd isotope data from the same samples are from Paces et al. (1991) and Snyder et al. (1994). The calculated sources for the data for Unruh Apollo (Ap) samples are from Unruh et al. (1984). Crystallization ages for each of the respective samples measured are listed in Beard et al. (1998), and Unruh et al. (1984). Three hypothetical mixing lines are shown from mixing between Apollo 12 ilmenite (ILM), Apollo 11 and 17 Hi–Ti, and KREEP lunar sources.

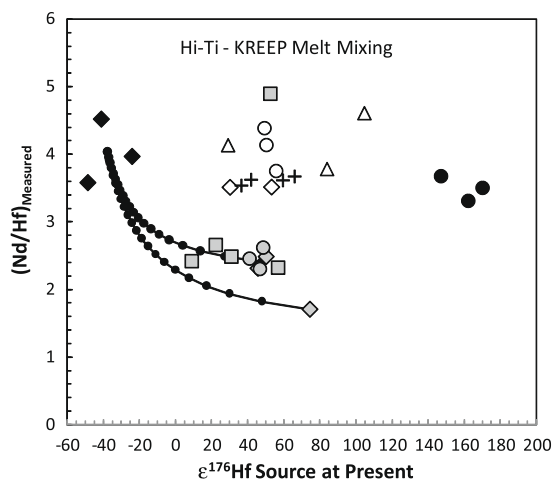


Fig. 7. The  $(\text{Nd}/\text{Hf})_{\text{Measured}}$  versus  $\epsilon^{176}\text{Hf}$  source at present using the depleted model in Figs. 5C and 6, for all lunar mare basalt samples measured to present. Mixing lines between average KREEP and the Hi-Ti samples 74275 and 70017 measured in this study are shown, with the dots in each mixing line representing 5% increments in the mixtures. All data sources are referenced in Fig. 6.

relationships,  $(\text{Nd}/\text{Hf})_{\text{Measured}}$  versus the calculated  $\epsilon^{176}\text{Hf}$  for the source at present is plotted (Fig. 7). With the exception of one Hi-Ti mare basalt where the fractions measured of the sample for Lu-Hf (10044,634, Beard et al., 1998), and Sm-Nd (10044,628, Snyder et al., 1994) were different, the Hi-Ti samples have  $(\text{Nd}/\text{Hf})_{\text{Measured}}$  ranging from 1.6 to 2.7, and significantly lower than those for Lo-Ti at 3.5–4.5 (Fig. 7). Mixtures between two Hi-Ti basalts and KREEP basalts, representing melt mixing, cannot explain the higher  $(\text{Nd}/\text{Hf})_{\text{Measured}}$  for the Lo-Ti samples as well as for several other petrologic types of mare basalts (Fig. 7). In a comprehensive examination of magmatic differentiation, mixing, and polybaric partial melting models, similar conclusions were reached by Beard et al. (1998), where they demonstrated that no viable mixing process explain the distinct Sm-Nd and Lu-Hf isotope systematics as a direct link between Lo-Ti and Hi-Ti mare basalts. Hence, the sources and magmatic histories for these two suites of rocks are independent of each other. The observed variability of Sm-Nd and Lu-Hf isotope systematics may reflect small and variable amounts of evolved trapped liquid in their different mantle sources, possibly derived from the last stages of magma ocean crystallization (Beard et al., 1998; Rankenburg et al., 2007; Debaille et al., 2008). These relationships indicate that mixing cannot explain the strong correlation between KREEP, Lo-Ti, and Apollo 17 Hi-Ti basalts for  $\mu^{142}\text{Nd}$  and  $\epsilon^{143}\text{Nd}$  (Fig. 5). This line, within the resolution of the multidynamic Nd isotope data, is best explained as being an isochron of  $\sim 229^{+24}_{-20}$  Ma<sub>ONC</sub> depending on model parameters.

## 7. IMPLICATIONS FOR EARLY MOON EVOLUTION

Two recent studies on  $^{142}\text{Nd}$ – $^{143}\text{Nd}$  of mare basalts (Boyett and Carlson, 2007) and  $^{176}\text{Hf}/^{177}\text{Hf}$  isotope ratio measurements of zircons with well-constrained ages from three

polymict breccia lunar highland rocks (Taylor et al., 2009) argue that the KREEP source formed as early as 4.44 Ga and  $4.476 \pm 0.047$  Ga ( $1\sigma$ ), respectively. In such a case, the KREEP formation would represent the last stages of crystallization of a lunar magma ocean as early as 4.523 Ga ( $\sim 46$  Ma<sub>ONC</sub>) and as late as 4429 Ga ( $\sim 140$  Ma<sub>ONC</sub>). These interpretations are consistent with the second model above, where the Moon formed from material with a superchondritic Sm/Nd ratio and the sources for other mare basalts, such as Hi-Ti and Lo-Ti, formed by additional differentiation possibly as late at 4.3 Ga. This early KREEP source formation time is appealing for several reasons. First, the most recent W isotope data for the Moon now shows it to have identical  $\epsilon^{182}\text{W}$  for the Earth (Touboul et al., 2007, 2009). This would give a mean accretion age for the Moon at no earlier than 4.517 Ga (52 Ma<sub>ONC</sub>) to no later than 4.417 Ga (152 Ma<sub>ONC</sub>; Touboul et al., 2007, 2009; Bourdon et al., 2008; Halliday, 2008). Solidification of a global-scale magma ocean as early as 4.44 Ga ( $\sim 129$  Ma<sub>ONC</sub>) as constrained by KREEP source formation at this time (Boyett and Carlson, 2007), would reduce the crystallization time to a maximum of  $\sim 60$ – $80$  Ma after accretion of the Moon and possibly much less (Taylor et al., 2009). Second, the early-formed crust defined by ages for ferroan anorthosites, likely resulting from plagioclase flotation after more than 50% magma ocean crystallization, is as old as  $4.46 \pm 0.04$  Ga (Norman et al., 2003). This age for crustal formation is also likely consistent with an early solidification of a lunar magma ocean. Both of these observations are consistent with a more rapid lunar magma ocean crystallization than a model for differentiation of 4.340 Ga of Fig. 5C. Hence, early-formed KREEP, and early magma ocean solidification, are consistent with a scenario where cooling is more rapid as a result of impact driven fracturing of the crust, keeping it from being an efficient insulator (Shearer and Newsom, 2000).

However, a KREEP reservoir formed as early as 4.44 Ga may be problematic for several reasons. First, the linear relationship between the six samples in this study for  $^{142}\text{Nd}$ – $^{143}\text{Nd}$ , verifying previous results for lunar basalt samples, requires KREEP as an end-member for mixing with Hi-Ti basalt source in order to generate Lo-Ti Nd isotope systematics, if the sources for these three mare basalt types did not form at the same time (Fig. 5B). However, as shown above, this mixing relationship is unlikely if one considers the coupled Hf-Nd systematics (Fig. 7), unless the calculated sources for the  $^{142}\text{Nd}$ – $^{143}\text{Nd}$  data of the six samples coincidentally lie on a well-correlated line for unknown reasons. Second, the uncertainty for the age of the KREEP source based on the Hf isotopic compositions of lunar zircons at  $4.476 \pm 0.047$  Ga is only calculated at  $\pm 1\sigma$  (Taylor et al., 2009). Taking a  $\pm 2\sigma$  uncertainty, or a 95.5% confidence interval, allows the formation age for the KREEP source from these data to be as young as 4.38 Ga, and approaching the age of  $4.340^{+0.024}_{-0.020}$  Ga ( $2\sigma$ ) for the  $^{142}\text{Nd}$ – $^{143}\text{Nd}$  isochron in Fig. 5C. Hence, these data are not inconsistent with a KREEP source formed as late as that obtained from the third  $^{142}\text{Nd}$ – $^{143}\text{Nd}$  model.

Boyett and Carlson (2007) in part based their interpretation of an early-formed KREEP reservoir and early crystal-

lization of the lunar magma ocean on the  $^{142}\text{Nd}$ – $^{143}\text{Nd}$  systematics of three crustal rocks measured to date. They noted that to account for initial  $\mu^{142}\text{Nd}$  relative to CHUR for two samples they measured – a 4.44 Ga ferroan anorthosite 60025 of +27 ppm, a 4.44 Ga hi-Mg suite norite 78326 of +24, and one sample – a 4.29 Ga ferroan anorthosite 62236 of +53 from Borg et al. (1999), requires a minimum differentiation age of the Moon of 4.45 Ga. Taken at face value, these three data require a Moon at 4.45 Ga with a  $^{147}\text{Sm}/^{144}\text{Nd}$  ratio of 0.23 that undergoes differentiation to produce a KREEP reservoir with a  $^{147}\text{Sm}/^{144}\text{Nd}$  ratio of 0.166 and an even more depleted reservoir with a  $^{147}\text{Sm}/^{144}\text{Nd}$  ratio of 0.263 to account for the initial  $\mu^{142}\text{Nd}$  relative to CHUR of sample 62,236 of Borg et al. (1999). However, a word of caution is suggested. These measurements were performed statically, with the potential inherent inaccuracy problems that may occur at 10 ppm or greater using this technique as discussed earlier. In addition, the very large  $^{142}\text{Nd}/^{144}\text{Nd}$  measured by Borg et al. (1999) was performed on a previous generation TIMS. At best this measurement has an associated error, based on  $\pm 2\sigma$  reproducibility of their standards of  $\pm 25$  ppm (Nyquist et al., 1995; Borg et al., 1999). Further, sample 66236 from Borg et al. (1999) had two measurements for  $\epsilon^{149}\text{Sm}$  of  $-30.8$  and  $-35.8$ , respectively. They applied a +28.8 ppm correction to their two measured  $^{142}\text{Nd}/^{144}\text{Nd}$  ratios based on  $\sigma_{\text{eff}}$  of  $^{149}\text{Sm}$  of 41,000 barns, consistent with the correction applied model 4 of Table 5, to the samples listed and using the Lingenfelter et al. (1972)  $\sigma_{\text{eff}}$  of  $^{149}\text{Sm}$  of 41,800 barns. Applying the correction preferred in this study with  $\sigma_{\text{eff}}$  of  $^{149}\text{Sm}$  of 71,267 barns, and  $\Psi/\mathcal{E} = 1.1$  (Table 5, model 1), gives a correction of +14.4 and +16.8, to the two Borg et al. (1999) measurements and hence, the stated initial value should be around 15.5 ppm lower at initial  $\mu^{142}\text{Nd}$  relative to CHUR of approximately +37. Taking this value and accepting the errors involved, all three crustal rocks may be adequately explained by a Moon having a  $^{147}\text{Sm}/^{144}\text{Nd}$  of 0.2136 as in Fig. 5C, and a differentiation age of 4.34 Ga to produce a KREEP source with  $^{147}\text{Sm}/^{144}\text{Nd}$  of  $\sim 0.15$ – $0.16$  and complementary superchondritic  $^{147}\text{Sm}/^{144}\text{Nd}$  reservoirs (Fig. 4b of Boyet and Carlson, 2007). It is suggested that additional multidynamic measurements will be needed to determine whether these important values on the crustal rocks are accurate to further examine these issues.

While an early formation of KREEP and a non-isochronous relationship for the line between KREEP, Lo–Ti, and Hi–Ti sources (Fig. 5) is appealing for reasons stated above, the problems with a mixing relationship between sample sources suggest that the most straight-forward mechanism to account for the strong correlation is that the sources for these samples all formed about the same time. Within the precision of the data and the assumptions of the models at present, the best age for the isochron is  $4.340^{+0.024}_{-0.020}$  Ga ( $\sim 229^{+24}_{-20}$  Ma<sub>ONC</sub>). Additional precision in the data must be reached in order to further examine validity of the time resolution of the determined age. However, this age allows for formation of the three source regions of these mare basalts over a maximum interval of 44 Ma. If this represents complete solidification of a lunar

magma ocean that was initiated by lunar accretion, it likely requires a longer cooling history than some models suggest (e.g. Shearer and Newsom, 2000). Evidence for a potentially more protracted cooling history has been recently advocated by the ages of zircons from lunar anorthositic breccias. The U–Pb age of  $4.417 \pm 0.006$  and younger from zircons in breccia 72,215 shows that anorthosites and KREEP melt components were being produced on timescales of 100 Ma or more after the formation and accretion of the Moon (Nemchin et al., 2009). Based on the established chronology of early-formed lunar materials, Nemchin et al. (2009) model the lunar magma ocean solidification with a decreasing exponential rate with time, from 100% melt at the Moon formation time of  $\sim 4.517$  Ga (W isotopes, Touboul et al., 2007), to 30% melt at the mean age of formation time of olivine-pyroxene-bearing cumulates at  $4.46 \pm 0.06$  Ga ( $^{147}\text{Sm}$ – $^{143}\text{Nd}$  isotopes, Norman et al., 2003), to a 5–7% melt or residual KREEP melt at the age of  $4.417 \pm 0.006$  Ga, and as much as 2–3% melt for possibly another 200–400 Ma, as shown by the young age distributions of their zircons. In this model for lunar magma ocean crystallization, small amounts of melt could pervade the source regions of KREEP, Lo–Ti, and Hi–Ti until a Sm–Nd closure time of  $\sim 4.34$  Ga that is obtained from the coupled  $^{142}\text{Nd}$ – $^{143}\text{Nd}$  systematics presented here and previously (Nyquist et al., 1995; Rankenburg et al., 2006; Boyet and Carlson, 2007). This scenario can also explain the Sm–Nd and Lu–Hf isotope variation of lunar mare basalts via late-stage melt addition in their source regions as noted above (Beard et al., 1998; Rankenburg et al., 2007; Debaille et al., 2008), and is consistent with the expectation of variable mixing between evolved melts and cumulates in a turbulent but nearly-solidified magma ocean (Tonks and Melosh, 1990). Such a scenario may be consistent with a thick plagioclase crust acting as an insulating barrier to heat transport (Solomon and Longhi, 1977). Alternatively, the 4.34 Ga age may represent a large-scale mantle overturn (Ringwood and Kesson, 1976; Spera, 1992; Hess and Parmentier, 1995; Elkins-Tanton et al., 2002) or mixing processes as yet to be determined (Bourdon et al., 2008; Jacobsen et al., 2008). In either case, this model will require that the mantle sources for the lunar mare basalts closed at a time later than the earliest formed lunar crust.

## 8. IMPLICATIONS FOR THE EARTH–MOON Sm/Nd

The models presented here based on  $\mu^{142}\text{Nd}$ – $\epsilon^{143}\text{Nd}$ – $\epsilon^{176}\text{Hf}$  systematics of the KREEP, Lo–Ti, and Hi–Ti lunar basalts measured, have implications to the Earth–Moon system. A key implication is that the Moon must have had a superchondritic Sm/Nd ratio when it formed. This was previously suggested (Boyet and Carlson, 2007; Caro et al., 2008). Based on the data from this study, the best model to explain the coupled  $^{142}\text{Nd}$ – $^{143}\text{Nd}$ – $^{176}\text{Hf}$  isotope relationships is shown in Fig. 5C, which includes a Sm/Nd fractionation event from chondritic ratios at 31 Ma<sub>ONC</sub> leading to a  $^{147}\text{Sm}/^{144}\text{Nd}$  of  $\sim 0.2136$ . Such a  $^{147}\text{Sm}/^{144}\text{Nd}$  ratio for the Moon is consistent with the estimate of  $\sim 0.211$  for a model of Sm/Nd fractionation at 250 Ma<sub>ONC</sub> developed by Boyet and Carlson

(2007). This model predicts that the Sm/Nd ratio of the system was likely established early in solar system history, prior to or around the time of the giant impact that formed the Moon. This estimate would imply that the Earth and Moon, which are the hybrid, and likely well-homogenized mixture of proto-Earth and a Mars-sized impactor (Pahlevan and Stevenson, 2007), had a  $^{147}\text{Sm}/^{144}\text{Nd}$  of  $\sim 0.2136$  at the time of the impact such that it was inherited prior to this Moon-forming event. If proto-Earth and the Mars-sized impactor underwent early differentiation from bulk chondritic material, an enriched reservoir is necessary with a subchondritic Sm/Nd ratio to counterbalance the superchondritic Sm/Nd of the post collision Earth and Moon. This reservoir would have not participated in producing the Moon.

Three possible scenarios can account for an early superchondritic Sm/Nd ratio established prior to the final stages of accretion (Carlson and Boyet, 2008). In one scenario, collisional erosion of crust with a superchondritic Sm/Nd ratio may have occurred on differentiated small bodies up to the size of planetesimals that then accrete to form larger planets (O'Neill and Palme, 2008). Highly energetic collisions that could result in removal of low Sm/Nd crust after the earliest accretion of km-sized objects in the first few million years of solar system formation and final accretion of planet-sized objects from 30 to 70  $\text{Ma}_{\text{ONC}}$ . Such a mechanism appears to explain the evidence for post-nebular volatilization, as well as a many of the bulk chemical characteristics of the present-day Earth (O'Neill and Palme, 2008). O'Neill and Palme (2008) postulated that a depletion of 6% in  $^{147}\text{Sm}/^{144}\text{Nd}$  to a value of 0.211 relative to average chondrites, could have been achieved by removal of around half of the 2.6% of crust expected to form from the silicate portions of terrestrial planetesimals. The timing of this model would be consistent with model presented in Fig. 5C, that requires a Sm/Nd fractionation event at around 31  $\text{Ma}_{\text{ONC}}$  and likely prior to formation of the Moon at around 60  $\text{Ma}_{\text{ONC}}$  or later.

In a second scenario explosive volcanism in the form of basaltic pyroclastic material escaping gravitational pull on planetesimals can reconcile the observation of having no plagioclase-bearing material (i.e. basaltic) genetically related to ultramafic restites such as ureilites and aubrites, in the meteorite collections (Warren, 2008). Such a mechanism of 'crust' loss may equally explain an Earth–Moon system with superchondritic Sm/Nd ratios. However, while this mechanism may have operated in early-formed small terrestrial bodies, because these bodies undergo rapid differentiation within the first few million years of solar system formation, this Sm/Nd fractionation event would have taken place well before the 31  $\text{Ma}_{\text{ONC}}$  postulated in the model presented in Fig. 5C.

In a third scenario, the superchondritic Sm/Nd for the Moon may result from chondrule size sorting in the inner solar system prior to accretion into larger objects (Caro et al., 2008). Bourdon et al. (2008) suggested that the average  $^{147}\text{Sm}/^{144}\text{Nd}$  ratio for chondrules is higher than average bulk chondrites with  $^{147}\text{Sm}/^{144}\text{Nd} = 0.1964$ , although they note that additional chondrule data are required to examine this potential mechanism for explaining a superchondritic

Sm/Nd ratio for some terrestrial planets. The chondrule  $^{147}\text{Sm}/^{144}\text{Nd}$  values range from 0.1787 to 0.2283 with an average of 0.210 (Amelin and Rotenberg, 2004). This would imply that the material building Earth and the Moon would have contained a large percentage of high  $^{147}\text{Sm}/^{144}\text{Nd}$  ratio chondrules via a sorting mechanism. This mechanism also requires an earlier time of Sm/Nd fractionation than the  $\sim 31 \text{ Ma}_{\text{ONC}}$  of collisional erosion. With the regression of the data for  $\mu^{142}\text{Nd} - \epsilon^{143}\text{Nd}$  in Fig. 5B and C, the time resolution for early Sm/Nd fractionation, i.e., the intersection point for  $\epsilon^{143}\text{Nd}$  for the source at present and  $\mu^{142}\text{Nd} = 0$  with a depleted model isochron for Sm/Nd fractionation, is uncertain enough to accommodate a much younger than 31  $\text{Ma}_{\text{ONC}}$  age near the time of solar system formation and at the time of or prior to material accretion into km-sized objects. Hence, the second and third scenarios cannot be ruled out with the current time resolution for early Sm/Nd fractionation for models derived from the new Nd isotope data lunar basalts. While additional multidynamic Nd isotope data for lunar basalts will be required to resolve this, it is argued here that the models, and in particular, the depleted model in Fig. 5C, are most consistent with collisional erosion because of where the intersection of the multidynamic Nd isotope data is with respect to the depleted model isochrons for an early Sm/Nd fractionation, at around 31  $\text{Ma}_{\text{ONC}}$ .

Two additional implications arise for an Earth with a bulk superchondritic Sm/Nd ratio. First, there is no need to have an early-formed enriched reservoir with subchondritic Sm/Nd ratios to counterbalance to a chondritic Sm/Nd ratio in the present-day Earth. That such a reservoir existed in the Hadean is documented by the maximum  $\mu^{142}\text{Nd}$  of +20 ppm for 3.85 Ga West Greenland samples, that progressively decreases to +10 at 3.65 Ga (Bennett et al., 2007). These data indicate mixing of an early-formed subchondritic Sm/Nd reservoir back into the Hadean convecting mantle. The fact that no Earth samples have been found with initial  $\mu^{142}\text{Nd} < -20$  in post-Hadean rocks, is consistent with efficient mixing and essentially removal of this early-formed reservoir over time. One potential caveat to this scenario is the discovery of 1.42 Ga lithospheric mantle-derived Khariar alkaline rocks from India with  $\mu^{142}\text{Nd} = -8$  to  $-13$  (Upadhyay et al., 2009). These samples show that some remnant vestiges of the early-formed sub-terrestrial standard reservoir material existed at least well past Archean times. Whether enough of this material is still present in the Earth than can balance it bulk to average chondritic  $\mu^{142}\text{Nd} = -20$  is a subject of further examination. We consider it to be unlikely given that all modern samples measured to present, cluster at  $\mu^{142}\text{Nd} = 0$ . Such a scenario is thus consistent with a bulk Earth with a superchondritic Sm/Nd.

Second, if the bulk Earth and Moon  $^{147}\text{Sm}/^{144}\text{Nd}$  ratio is 0.2136, calculated from the model presented in Fig. 5C for the Moon, this means that the convecting mantle represented by the average MORB source has not changed in its bulk Sm/Nd ratio since the formation of the Earth. Thus, any igneous processes that have formed continents require a second superchondritic Sm/Nd reservoir to mass balance their subchondritic Sm/Nd. This conclusion was also

reached by Brandon et al. (2007) to account for the  $^{142}\text{Nd}$ – $^{143}\text{Nd}$  systematics of modern terrestrial ocean basalts. Additional multidynamic Nd data for lunar basalts will be required to further test this scenario and to determine if the preferred model presented in Fig. 5C is valid.

## 9. CONCLUSIONS

Six lunar basalts samples, ranging in bulk composition from Hi–Ti, Lo–Ti, and KREEP were measured for Sm–Nd and Lu–Hf isotope compositions. Evaluation of the new multidynamic data for high-precision  $^{142}\text{Nd}$  and  $^{143}\text{Nd}$  isotopes presented in this study, combined with static and multidynamic data from Rankenburg et al. (2006) and Boyet and Carlson (2007) shows the following. First, the averages for static  $\mu^{142}\text{Nd}$  obtained for three separate lines in the multidynamic runs for each sample in this study correlate on a 1:1 line with the averages of  $\mu^{142}\text{Nd}$  obtained multidynamically, indicating no within run analytical artifacts between the two different methods for measuring Nd isotopes during two distinct analytical campaigns in which these data were obtained. Second, the multidynamic Nd isotope data independently obtained in this study and in Boyet and Carlson (2007) on the same samples and on petrologically similar KREEP samples, correlate well at a precision of  $\pm 5$  ppm ( $2\sigma$ ) or better, which is within external precision of the measurements for the Boyet and Carlson (2007) study. Third the static data from Rankenburg et al. (2006) and Boyet and Carlson (2007) also correlate with the separate sets of multidynamic data obtained on the two Triton TIMS in this study and Boyet and Carlson (2007), respectively, but each regression line for the two comparisons is displaced from and at angles to a 1:1 line. This means some samples measured by static deviate from their values obtained multidynamically for each study by more than 10 ppm and beyond the stated external precisions defined by multiple standard measurements. This analysis demonstrates that high-precision Nd isotope measurements should be performed using multidynamic routines that are empirically shown here to more accurately reproduce the Nd isotopic compositions of rock samples within the cited external and internal precisions.

Assessment of the corrections for neutron fluence in lunar rock samples indicates that the most robust neutron fluence corrections are based on using recent published thermal neutron cross sections and epithermal resonance integrals as employed by Rankenburg et al. (2006) which is adapted from Nyquist et al. (1995). In particular, using a  $^{149}\text{Sm}$   $\sigma_{\text{eff}}$  of 71,627 barns and a  $\Psi/\mathcal{E}$  of 1.1, the latter of which comes from a direct measurement on the Moon, results in more systematic, and thus in our view, more accurate Nd isotope compositions than does using  $^{149}\text{Sm}$   $\sigma_{\text{eff}}$  of 56,000 and 41,800 barns and variable  $\Psi/\mathcal{E}$  adapted in previous studies (Nyquist et al., 1995; Boyet and Carlson, 2007).

The model that best explains the Nd–Hf isotope compositions of the measured lunar mare basalts measured to present is one where the bulk Moon has a superchondritic  $^{147}\text{Sm}/^{144}\text{Nd}$  ratio ranging from about 0.209 to 0.2136, or 6% to 8.8% higher than the average for chondrites. The strong correlation between  $\mu^{142}\text{Nd}$ – $\epsilon^{143}\text{Nd}$  for the calcu-

lated sources for KREEP, Hi–Ti, and Lo–Ti samples cannot be explained as a mixing line if one considers combined Nd and Hf isotope compositions which indicate that there is no mixing between Hi- and Lo–Ti source regions. Instead, the correlation in  $^{142}\text{Nd}$ – $^{143}\text{Nd}$  isotope systematics is best interpreted to reflect an isochron with an age of  $229^{+24}_{-20}$  Ma after the onset of nebular condensation. In such a case, this indicates that the sources for these lunar mare basalts regions were closed with respect to these isotopic systems around 150–190 Ma following accretion of the Moon. This in turn implies either a protracted magma ocean cooling history or remobilization of their source regions at this time. Because of the uncertainty of the data, the isochron may best reflect a *circa* 44 Ma formation interval for the mantle sources rather than well-defined and more narrow time sequence of formation. A long cooling history of a magma ocean is consistent with U–Pb age distributions in zircons (Nemchin et al., 2009) and we prefer this process to account of for the observed 229 Ma isochron for  $^{142}\text{Nd}$ – $^{143}\text{Nd}$  systematics of the lunar mare basalts.

Because the best estimate for the  $^{147}\text{Sm}/^{144}\text{Nd}$  ratio of the bulk Moon is identical or similar to the bulk  $^{147}\text{Sm}/^{144}\text{Nd}$  ratio for the Earth’s convecting mantle as represented by MORB, the Earth’s convecting mantle may have remained relatively constant with respect to Sm–Nd isotope systematics over its history, despite well-established fractionations resulting from partial melting and input from crust recycling. If so, there is no need to call on a volumetrically significant ‘missing reservoir’ at present-time with a subchondritic  $^{147}\text{Sm}/^{144}\text{Nd}$  ratio to mass balance the Earth to chondritic. This inference is consistent with the documented progressive shift from higher  $\mu^{142}\text{Nd}$  to that of the terrestrial standard that the Earth’s mantle appears to have undergone from approximately 3.85 Ga to 3.4 Ga (Bennett et al., 2007). These combined observations instead indicate that a possible early-formed enriched reservoir was efficiently mixed back into the convecting mantle in the Archean. The superchondritic  $^{147}\text{Sm}/^{144}\text{Nd}$  ratio of the present-day Earth’s convecting mantle in combination with the inference from the bulk Moon and bulk Earth compositional similarity, means that an additional superchondritic  $^{147}\text{Sm}/^{144}\text{Nd}$  ratio reservoir is required to counter balance the subchondritic  $^{147}\text{Sm}/^{144}\text{Nd}$  ratio of continental crust. This reservoir is likely to have formed over Earth history in lock step with crust formation, and mostly after the time of extant  $^{146}\text{Sm}$ .

## ACKNOWLEDGMENTS

This work was supported by a NASA Cosmochemistry grant to A.D.B. NASA and the Swiss Natural History Museum are thanked for providing samples. Vickie Bennett is thanked for helping to jointly develop the multidynamic method for high-precision measurements with A.D.B. in 2006 on the JSC Triton and for measuring several standard runs listed in this paper in 2008 while in residence at JSC. Maud Boyet and Richard Carlson are thanked for allowing us to use their unpublished  $^{145}\text{Nd}/^{144}\text{Nd}$  on the lunar samples they obtained  $^{142}\text{Nd}/^{144}\text{Nd}$  for and presented in Boyet and Carlson (2007). We thank Minako Righter for assistance in the clean laboratory at the University of Houston. We thank Richard Carlson, Mathieu Touboul, and Mukul Sharma for constructive journal reviews.

## APPENDIX A

All measured data obtained in this study for unspiked Nd runs. For the  $\mu$  values, the samples are normalized to the averages for the standards in each separate analytical campaign.

Campaign 1	$^{142}\text{Ce}$ ppm	Line 1 Static $^{142}\text{Nd}/^{144}\text{Nd}$	$\pm 2\sigma$	$\mu^{142}\text{Nd}$	$\pm 2\sigma$ ppm	Line 2 Static $^{142}\text{Nd}/^{144}\text{Nd}$	$\pm 2\sigma$	$\mu^{142}\text{Nd}$	$\pm 2\sigma$ ppm	Line 3 Static $^{142}\text{Nd}/^{144}\text{Nd}$	$\pm 2\sigma$	$\mu^{142}\text{Nd}$	$\pm 2\sigma$ ppm	Campaign 1	Multi-dyn. $^{142}\text{Nd}/^{144}\text{Nd}$	$\pm 2\sigma$	$\mu^{142}\text{Nd}$	$\pm 2\sigma$ ppm	Campaign 1
Ames 1-1	0.2	1.1418281	0.0000051	-1.5	4.5	1.1418503	0.0000050	-1.5	4.4	1.1418300	0.0000044	-2.4	3.9	Ames 1-1	1.1418396	0.0000026	0.2	2.3	Ames 1-1
Ames 1-2	0.0	1.1418301	0.0000046	0.3	4.0	1.1418526	0.0000043	0.6	3.8	1.1418363	0.0000047	3.2	4.1	Ames 1-2	1.1418385	0.0000025	-0.7	2.2	Ames 1-2
Ames 1-3	0.3	1.1418309	0.0000056	1.0	4.9	1.1418599	0.0000052	6.9	4.6	1.1418347	0.0000058	1.8	5.1	Ames 1-3	1.1418410	0.0000030	1.5	2.6	Ames 1-3
Ames 1-4	0.1	1.1418280	0.0000047	-1.6	4.1	1.1418519	0.0000044	-0.1	3.9	1.1418337	0.0000049	0.9	4.3	Ames 1-4	1.1418387	0.0000026	-0.6	2.3	Ames 1-4
Ames 1-5	1.0	1.1418236	0.0000045	-5.4	3.9	1.1418501	0.0000047	-1.6	4.1	1.1418343	0.0000046	1.4	4.0	Ames 1-5	1.1418371	0.0000026	-2.0	2.3	Ames 1-5
Ames 1-6	0.6	1.1418348	0.0000054	4.4	4.7	1.1418506	0.0000063	-1.2	5.5	1.1418337	0.0000061	0.9	5.3	Ames 1-6	1.1418405	0.0000031	1.0	2.7	Ames 1-6
Ames 1-7	0.6	1.1418298	0.0000038	0.0	3.3	1.1418477	0.0000039	-3.7	3.4	1.1418321	0.0000037	-0.5	3.2	Ames 1-7	1.1418368	0.0000019	-2.2	1.7	Ames 1-7
Ames 1-8	0.8	1.1418291	0.0000034	-0.6	3.0	1.1418536	0.0000034	-1.4	3.0	1.1418311	0.0000034	-1.4	3.0	Ames 1-8	1.1418382	0.0000018	-1.0	1.6	Ames 1-8
Ames 1-9	0.5	1.1418311	0.0000034	1.1	3.0	1.1418512	0.0000035	-0.7	3.1	1.1418340	0.0000034	1.1	3.0	Ames 1-9	1.1418387	0.0000019	-0.6	1.7	Ames 1-9
Ames 1-10	0.3	1.1418326	0.0000051	2.4	4.5	1.1418518	0.0000057	-0.1	5.0	1.1418271	0.0000060	-4.9	5.3	Ames 1-10	1.1418404	0.0000028	0.9	2.5	Ames 1-10
LaJolla 1-1	0.4	1.1418320	0.0000048	1.9	4.2	1.1418491	0.0000046	-2.5	4.0	1.1418368	0.0000047	3.6	4.1	LaJolla 1-1	1.1418398	0.0000024	0.4	2.1	LaJolla 1-1
LaJolla 1-2	0.1	1.1418275	0.0000043	-2.0	3.8	1.1418542	0.0000048	2.0	4.2	1.1418358	0.0000042	2.7	3.7	LaJolla 1-2	1.1418395	0.0000026	0.1	2.3	LaJolla 1-2
LaJolla 1-3	0.3	1.1418289	0.0000050	-0.8	4.4	1.1418556	0.0000054	3.2	4.7	1.1418349	0.0000052	1.9	4.6	LaJolla 1-3	1.1418394	0.0000030	0.1	2.6	LaJolla 1-3
LaJolla 1-4	0.1	1.1418222	0.0000050	-6.7	4.4	1.1418478	0.0000047	-3.7	4.1	1.1418392	0.0000049	5.7	4.3	LaJolla 1-4	1.1418384	0.0000027	-0.8	2.4	LaJolla 1-4
LaJolla 1-5	1.3	1.1418230	0.0000055	-6.0	4.8	1.1418570	0.0000060	4.4	5.3	1.1418388	0.0000060	5.3	5.3	LaJolla 1-5	1.1418395	0.0000030	0.1	2.6	LaJolla 1-5
<b>Campaign 2</b>																			
Ames 2-1	0.6	1.1418519	0.0000045	3.0	3.9	1.1418364	0.0000048	8.9	4.2	1.1418389	0.0000044	-0.4	3.9	Ames 2-1	1.1418429	0.0000025	3.1	2.2	Ames 2-1
Ames 2-2	0.1	1.1418505	0.0000045	1.8	3.9	1.1418300	0.0000046	3.3	4.0	1.1418420	0.0000045	2.3	3.9	Ames 2-2	1.1418403	0.0000025	0.8	2.2	Ames 2-2
Ames 2-3	0.9	1.1418460	0.0000045	-2.2	3.9	1.1418227	0.0000044	-3.1	3.9	1.1418454	0.0000045	5.3	3.9	Ames 2-3	1.1418398	0.0000023	0.4	2.0	Ames 2-3
Ames 2-4	0.2	1.1418527	0.0000050	3.7	4.4	1.1418250	0.0000045	-1.1	3.9	1.1418420	0.0000048	2.3	4.2	Ames 2-4	1.1418398	0.0000025	0.4	2.2	Ames 2-4
Ames 2-5	0.3	1.1418408	0.0000057	-6.7	5.0	1.1418168	0.0000054	-8.2	4.7	1.1418305	0.0000052	-7.8	4.6	Ames 2-5	1.1418377	0.0000028	-1.4	2.5	Ames 2-5
Ames 2-6	0.5	1.1418476	0.0000068	-0.8	6.0	1.1418236	0.0000053	-2.3	4.6	1.1418382	0.0000054	-1.0	4.7	Ames 2-6	1.1418395	0.0000029	0.1	2.5	Ames 2-6
Ames 2-7	0.2	1.1418497	0.0000051	1.1	4.5	1.1418289	0.0000050	2.4	4.4	1.1418385	0.0000048	-0.8	4.2	Ames 2-7	1.1418400	0.0000026	0.6	2.3	Ames 2-7
LaJolla 2-1	0.6	1.1418499	0.0000052	1.3	4.6	1.1418311	0.0000050	4.3	4.4	1.1418324	0.0000051	-6.1	4.5	LaJolla 2-1	1.1418394	0.0000028	0.1	2.5	LaJolla 2-1
LaJolla 2-2	0.2	1.1418423	0.0000051	-5.4	4.5	1.1418325	0.0000047	5.5	4.1	1.1418382	0.0000051	-1.0	4.5	LaJolla 2-2	1.1418387	0.0000027	-0.6	2.4	LaJolla 2-2
<b>AVERAGES</b>																			
AMES Camp 1		1.1418298	0.0000060	0.9	5.3	1.1418520	0.0000064	-0.2	5.6	1.1418327	0.0000054	-1.3	4.7	AMES Camp 1	1.1418390	0.0000028	0.3	2.5	AMES Camp 1
La Jolla Camp 1		1.1418267	0.0000082	-1.8	7.2	1.1418527	0.0000081	0.4	7.1	1.1418371	0.0000037	2.6	3.3	La Jolla Camp 1	1.1418400	0.0000031	-0.6	2.7	La Jolla Camp 1
Campaign 1		1.1418288	0.0000072	0.0	6.3	1.1418522	0.0000068	0.0	5.9	1.1418342	0.0000064	0.0	5.6	La Jolla Camp 1	1.1418393	0.0000011	-0.3	0.9	AMES All
AMES Camp 2		1.1418485	0.0000082	0.5	7.2	1.1418262	0.0000125	-1.1	11.0	1.1418394	0.0000094	0.8	8.2	La Jolla Camp 2	1.1418391	0.0000010	-0.0	0.9	AMES All
La Jolla Camp 2		1.1418461	0.0000107	-1.6	9.4	1.1418318	0.0000020	3.8	1.7	1.1418353	0.0000082	-2.8	7.2	Campaign 1	1.1418391	0.0000024	-0.2	2.1	La Jolla Camp 1
Campaign 2		1.1418479	0.0000083	0.0	7.3	1.1418274	0.0000119	0.0	10.4	1.1418385	0.0000093	0.0	8.2	Campaign 2	1.1418398	0.0000028	0.4	2.5	La Jolla Camp 2
All														All	1.1418393	0.0000026	0.0	2.3	La Jolla All
<b>Lunar Samples</b>																			
KREEP														KREEP					KREEP
SAU169-1-1	0.6	1.1417930	0.0000060	-31.3	5.3	1.1418307	0.0000058	-18.9	5.1	1.1418067	0.0000062	-24.1	5.4	SAU169-1-1	1.1418101	0.0000033	-25.4	2.9	SAU169-1-1
SAU 169-1-2	2.0	1.1417979	0.0000040	-27.0	3.5	1.1418247	0.0000042	-24.1	3.7	1.1418084	0.0000043	-22.6	3.8	SAU 169-1-2	1.1418101	0.0000025	-25.4	2.2	SAU 169-1-2
SAU 169-2-3	4.5	1.1418211	0.0000046	-23.5	4.0	1.1418035	0.0000043	-21.0	3.8	1.1418019	0.0000043	-32.0	3.8	SAU 169-2-3	1.1418080	0.0000022	-27.8	1.9	SAU 169-2-3
SAU 169-2-3.rpt	0.8	1.1418230	0.0000045	-21.8	3.9	1.1418006	0.0000046	-23.5	4.0	1.1418024	0.0000044	-31.6	3.9	SAU 169-2-3.rpt	1.1418092	0.0000024	-26.8	2.1	SAU 169-2-3.rpt
AVERAGE				-25.9	8.4			-21.9	4.8			-27.6	9.9	AVERAGE			-26.3	4.2	AVERAGE
15386-1-1	0.1	1.1417935	0.0000078	-30.9	6.8	1.1418216	0.0000088	-26.8	7.7	1.1418026	0.0000096	-27.6	8.4	15386-1-1	1.1418048	0.0000048	-30.0	4.4	15386-1-1
15386-1-2	0.8	1.1417897	0.0000037	-34.2	3.2	1.1418255	0.0000035	-23.4	3.1	1.1417976	0.0000034	-32.0	3.0	15386-1-2	1.1418037	0.0000021	-31.0	1.8	15386-1-2
15386-2-3	2.2	1.1418145	0.0000045	-29.3	3.9	1.1417909	0.0000045	-32.0	3.9	1.1418079	0.0000045	-26.8	3.9	15386-2-3	1.1418034	0.0000025	-31.9	2.2	15386-2-3
15386-2-3.rpt	0.3	1.1418134	0.0000043	-30.2	3.8	1.1417937	0.0000043	-29.6	3.8	1.1417982	0.0000041	-35.3	3.6	15386-2-3.rpt	1.1418040	0.0000024	-31.3	2.1	15386-2-3.rpt
AVERAGE				-31.2	4.3			-27.9	7.4			-30.4	7.9	AVERAGE			-31.1	1.6	AVERAGE
<b>Low-Ti</b>																			
LAP 02205-1-1	0.7	1.1418177	0.0000037	-9.7	3.2	1.1418497	0.0000045	-2.2	3.9	1.1418224	0.0000037	-10.3	3.2	LAP 02205-1-1	1.1418289	0.0000022	-8.9	1.9	LAP 02205-1-1
LAP 02205-2-2	3.8	1.1418405	0.0000045	-6.5	3.9	1.1418271	0.0000043	-0.3	3.8	1.1418217	0.0000047	-14.7	4.1	LAP 02205-2-2	1.1418305	0.0000023	-8.1	2.0	LAP 02205-2-2
LAP 02205-2-2.r	0.9	1.1418444	0.0000045	-3.1	3.9	1.1418239	0.0000049	-3.1	4.3	1.1418216	0.0000045	-14.8	3.9	LAP 02205-2-2.r	1.1418304	0.0000022	-8.2	1.9	LAP 02205-2-2.r
AVERAGE				-6.4	6.6			-13.2	5.1			-12.8	5.1	AVERAGE			-8.4	0.8	AVERAGE
15555-1-1	1.0	1.1418210	0.0000038	-6.8	3.3	1.1418511	0.0000040	-1.0	3.5	1.1418262	0.0000042	-7.0	3.7	15555-1-1	1.1418348	0.0000020	-3.7	1.8	15555-1-1
15555-2-2	0.4	1.1418452	0.0000045	-2.4	3.9	1.1418147	0.0000042	-11.2	3.7	1.1418241	0.0000043	-12.6	3.8	15555-2-2	1.1418305	0.0000024	-8.1	2.1	15555-2-2
AVERAGE				-4.6	6.3			-6.1	14.4			-9.8	7.9	AVERAGE			-5.9	6.2	AVERAGE
<b>High-Ti</b>																			
70017-1-1	0.6	1.1418410	0.0000045	10.7	3.9	1.1418728	0.0000049	18.0	4.3	1.1418497	0.0000040	13.6	3.5	70017-1-1	1.1418547	0.0000021	13.7	1.8	70017-1-1
70017-2-2	2.1	1.1418586	0.0000046	9.3	4.0	1.1418428	0.0000047	13.4	4.1	1.1418507	0.0000046	10.7	4.0	70017-2-2	1.1418547	0.0000026	13.1	2.3	70017-2-2
AVERAGE				10.0	1.9			15.7	6.5			12.2	4.1	AVERAGE			13.4	0.9	AVERAGE
74275-1-1	0.8	1.1418453	0.0000042	14.5	3.7	1.1418787	0.0000042	23.2	3.7	1.1418545	0.0000041	17.8	3.6	74275-1-1	1.1418585	0.0000022	17.0	1.9	74275-1-1
74275-1-2	1.9	1.1418465	0.0000066	15.5	5.8	1.1418724	0.0000062	17.7	5.4	1.1418500	0.0000063	13.9	5.5	74275-1-2	1.1418565	0.0000034	15.3	3.0	74275-1-2
74275-2-3	2.1	1.1418699	0.000006	19.2	5.1	1.1418474	0.000006	17.5	5.1	1.141857									

Multi-dyn. <sup>143</sup> Nd/ <sup>144</sup> Nd	±2σ	μ <sup>143</sup> Nd	±2σ ppm	Campaign 1	Multi-dyn. <sup>143</sup> Nd/ <sup>144</sup> Nd	±2σ	μ <sup>143</sup> Nd	±2σ ppm	Raw <sup>143</sup> Nd/ <sup>144</sup> Nd	Campaign 2	Multi-dyn. <sup>143</sup> Nd/ <sup>144</sup> Nd	±2σ	μ <sup>143</sup> Nd	±2σ ppm	Raw <sup>143</sup> Nd/ <sup>144</sup> Nd	Campaign 1	Multi-dyn. <sup>143</sup> Nd/ <sup>144</sup> Nd	±2σ	μ <sup>143</sup> Nd	±2σ ppm	Multi-dyn. <sup>143</sup> Nd/ <sup>144</sup> Nd	±2σ	μ <sup>143</sup> Nd	±2σ ppm	Static <sup>143</sup> Nd/ <sup>144</sup> Nd	±2σ	μ <sup>143</sup> Nd	±2σ ppm		
0.5121334	0.0000010	0.0	2.0	Ames 1-1	0.3484053	0.0000008	0.1	2.3	0.72171	Ames 1-1	0.2415780	0.0000009	2.9	3.7	0.72171	Ames 1-1	0.2415780	0.0000009	2.9	3.7	0.2364518	0.0000017	5.1	7.2	0.2364518	0.0000017	5.1	7.2		
0.5121337	0.0000011	0.0	2.0	Ames 1-2	0.3484053	0.0000007	3.0	2.0	0.72471	Ames 1-2	0.2415780	0.0000008	5.4	3.3	0.72471	Ames 1-2	0.2415780	0.0000008	5.4	3.3	0.2364542	0.0000017	15.2	7.2	0.2364542	0.0000017	15.2	7.2		
0.5121340	0.0000011	0.0	1.8	Ames 1-3	0.3484057	0.0000008	1.2	2.3	0.72180	Ames 1-3	0.2415780	0.0000009	2.5	3.7	0.72180	Ames 1-3	0.2415780	0.0000009	2.5	3.7	0.2364492	0.0000014	-0.8	5.9	0.2364492	0.0000014	-0.8	5.9		
0.5121344	0.0000012	0.0	1.8	Ames 1-4	0.3484057	0.0000008	1.2	2.3	0.72180	Ames 1-4	0.2415780	0.0000009	3.3	3.7	0.72180	Ames 1-4	0.2415780	0.0000009	3.3	3.7	0.2364508	0.0000017	0.8	7.2	0.2364508	0.0000017	0.8	7.2		
0.5121346	0.0000012	0.0	2.3	Ames 1-5	0.3484054	0.0000007	-1.9	2.0	0.72075	Ames 1-5	0.2415780	0.0000008	2.1	3.3	0.72075	Ames 1-5	0.2415780	0.0000008	2.1	3.3	0.2364532	0.0000019	11.0	8.0	0.2364532	0.0000019	11.0	8.0		
0.5121346	0.0000012	0.0	2.3	Ames 1-6	0.3484054	0.0000007	0.4	2.6	0.72216	Ames 1-6	0.2415780	0.0000001	4.1	0.4	0.72216	Ames 1-6	0.2415780	0.0000001	4.1	0.4	0.2364540	0.0000020	14.4	8.5	0.2364540	0.0000020	14.4	8.5		
0.5121346	0.0000012	0.0	1.4	Ames 1-7	0.3484055	0.0000005	-2.2	1.4	0.72112	Ames 1-7	0.2415780	0.0000007	-1.2	2.9	0.72112	Ames 1-7	0.2415780	0.0000007	-1.2	2.9	0.2364485	0.0000013	-8.9	5.5	0.2364485	0.0000013	-8.9	5.5		
0.5121337	0.0000007	0.0	1.4	Ames 1-8	0.3484055	0.0000005	-0.8	1.4	0.72138	Ames 1-8	0.2415782	0.0000006	-2.5	2.5	0.72138	Ames 1-8	0.2415782	0.0000006	-2.5	2.5	0.2364490	0.0000013	-6.8	5.5	0.2364490	0.0000013	-6.8	5.5		
0.5121335	0.0000007	0.0	1.4	Ames 1-9	0.3484055	0.0000005	-2.2	1.4	0.72143	Ames 1-9	0.2415784	0.0000006	-1.7	2.5	0.72143	Ames 1-9	0.2415784	0.0000006	-1.7	2.5	0.2364496	0.0000012	-4.2	5.1	0.2364496	0.0000012	-4.2	5.1		
0.5121335	0.0000011	0.0	2.1	Ames 1-10	0.3484052	0.0000006	-0.2	1.7	0.72160	Ames 1-10	0.2415776	0.0000008	-5.0	3.3	0.72160	Ames 1-10	0.2415776	0.0000008	-5.0	3.3	0.2364499	0.0000019	-19.9	8.0	0.2364499	0.0000019	-19.9	8.0		
0.5118459	0.0000011	-5.6	2.0	LaJolla 1-1	0.3484052	0.0000006	-0.2	1.7	0.72110	LaJolla 1-1	0.2415782	0.0000008	5.8	3.3	0.72110	LaJolla 1-1	0.2415782	0.0000008	5.8	3.3	0.2364536	0.0000017	12.7	7.2	0.2364536	0.0000017	12.7	7.2		
0.5118459	0.0000012	-5.6	2.3	LaJolla 1-2	0.3484044	0.0000008	-2.5	2.3	0.72322	LaJolla 1-2	0.2415826	0.0000009	15.7	3.7	0.72322	LaJolla 1-2	0.2415826	0.0000009	15.7	3.7	0.2364572	0.0000016	27.9	6.8	0.2364572	0.0000016	27.9	6.8		
0.5118455	0.0000009	-5.6	2.0	LaJolla 1-3	0.3484038	0.0000006	-4.2	2.3	0.72084	LaJolla 1-3	0.2415811	0.0000009	9.5	3.7	0.72084	LaJolla 1-3	0.2415811	0.0000009	9.5	3.7	0.2364549	0.0000018	18.2	7.6	0.2364549	0.0000018	18.2	7.6		
0.5118455	0.0000009	-5.6	1.8	LaJolla 1-4	0.3484051	0.0000008	-0.5	2.1	0.72133	LaJolla 1-4	0.2415823	0.0000010	14.5	4.1	0.72133	LaJolla 1-4	0.2415823	0.0000010	14.5	4.1	0.2364560	0.0000018	22.8	7.6	0.2364560	0.0000018	22.8	7.6		
0.5118465	0.0000012	-5.6	2.3	LaJolla 1-5	0.3484060	0.0000008	2.1	2.3	0.72074	LaJolla 1-5	0.2415810	0.0000010	9.1	4.1	0.72074	LaJolla 1-5	0.2415810	0.0000010	9.1	4.1	0.2364526	0.0000020	8.5	8.5	0.2364526	0.0000020	8.5	8.5		
0.5113358	0.0000010	0.0	2.0	Ames 2-1	0.3484028	0.0000007	-6.0	2.0	0.72155	Ames 2-1	0.2415780	0.0000008	-3.3	3.3	0.72155	Ames 2-1	0.2415780	0.0000008	-3.3	3.3	0.2364500	0.0000016	-2.5	6.8	0.2364500	0.0000016	-2.5	6.8		
0.5121345	0.0000010	0.0	2.0	Ames 2-2	0.3484027	0.0000007	-6.3	2.0	0.72430	Ames 2-2	0.2415780	0.0000008	0.4	3.3	0.72430	Ames 2-2	0.2415780	0.0000008	0.4	3.3	0.2364515	0.0000015	3.8	6.3	0.2364515	0.0000015	3.8	6.3		
0.5121349	0.0000010	0.0	1.8	Ames 2-3	0.3484035	0.0000007	-4.0	2.0	0.72110	Ames 2-3	0.2415780	0.0000009	-1.8	5.5	0.72110	Ames 2-3	0.2415780	0.0000009	-1.8	5.5	0.2364505	0.0000019	-0.5	8.1	0.2364505	0.0000019	-0.5	8.1		
0.5121349	0.0000010	0.0	1.8	Ames 2-4	0.3484028	0.0000007	-6.0	2.0	0.72375	Ames 2-4	0.2415780	0.0000009	-3.3	3.3	0.72375	Ames 2-4	0.2415780	0.0000009	-3.3	3.3	0.2364517	0.0000017	4.7	7.2	0.2364517	0.0000017	4.7	7.2		
0.5121340	0.0000009	0.0	1.8	Ames 2-5	0.3484026	0.0000006	-6.5	1.7	0.72253	Ames 2-5	0.2415785	0.0000008	-1.2	3.3	0.72253	Ames 2-5	0.2415785	0.0000008	-1.2	3.3	0.2364501	0.0000019	-2.1	8.0	0.2364501	0.0000019	-2.1	8.0		
0.5121344	0.0000010	0.0	1.8	Ames 2-6	0.3484031	0.0000006	-5.1	2.3	0.72120	Ames 2-6	0.2415778	0.0000010	-4.1	4.1	0.72120	Ames 2-6	0.2415778	0.0000010	-4.1	4.1	0.2364491	0.0000023	-6.3	9.7	0.2364491	0.0000023	-6.3	9.7		
0.5121346	0.0000010	0.0	2.0	Ames 2-7	0.3484030	0.0000007	-5.5	2.0	0.72391	Ames 2-7	0.2415785	0.0000009	-1.2	3.7	0.72391	Ames 2-7	0.2415785	0.0000009	-1.2	3.7	0.2364499	0.0000018	-3.0	7.6	0.2364499	0.0000018	-3.0	7.6		
0.5118463	0.0000010	-5.6	2.0	LaJolla 2-1	0.3484023	0.0000008	-7.4	2.3	0.72089	LaJolla 2-1	0.2415805	0.0000009	7.0	3.7	0.72089	LaJolla 2-1	0.2415805	0.0000009	7.0	3.7	0.2364549	0.0000017	18.2	7.2	0.2364549	0.0000017	18.2	7.2		
0.5118459	0.0000011	-5.6	2.1	LaJolla 2-2	0.3484022	0.0000007	-7.7	2.0	0.72362	LaJolla 2-2	0.2415801	0.0000008	5.4	3.3	0.72362	LaJolla 2-2	0.2415801	0.0000008	5.4	3.3	0.2364539	0.0000019	14.0	8.0	0.2364539	0.0000019	14.0	8.0		
0.5121337	0.0000012	0.0	2.4	Ames Camp 1	0.3484053	0.0000013	0.4	3.7		Ames Camp 1	0.2415790	0.0000016	1.0	6.7		Ames Camp 1	0.2415790	0.0000016	1.0	6.7	0.2364506	0.0000054	0.1	22.7	0.2364506	0.0000054	0.1	22.7		
0.5121346	0.0000012	0.0	1.0	La Jolla Camp 1	0.3484049	0.0000017	-0.7	4.8		Ames Camp 2	0.2415784	0.0000015	0.0	6.2		Ames All	0.2415784	0.0000015	0.0	6.2	0.2364505	0.0000042	0.0	17.8	0.2364505	0.0000042	0.0	17.8		
0.5121349	0.0000010	0.0	1.0	Campaign 1	0.3484051	0.0000014	0.0	4.1		Ames All	0.2415788	0.0000015	0.0	6.2																
0.5118458	0.0000009	-5.6	1.8	Ames Camp 2	0.3484029	0.0000006	0.4	1.7		La Jolla Camp 1	0.2415814	0.0000020	10.9	8.2		La Jolla Camp 1	0.2415814	0.0000020	10.9	8.2	0.2364549	0.0000037	18.0	15.5	0.2364549	0.0000037	18.0	15.5		
0.5118461	0.0000006	-5.6	1.1	La Jolla Camp 2	0.3484023	0.0000001	-1.5	0.4		La Jolla Camp 2	0.2415803	0.0000006	6.2	2.3		La Jolla Camp 2	0.2415803	0.0000006	6.2	2.3	0.2364544	0.0000014	16.1	6.0	0.2364544	0.0000014	16.1	6.0		
0.5118459	0.0000004	-5.6	0.8	Campaign 2	0.3484028	0.0000008	0.0	2.3		La Jolla All	0.2415811	0.0000020	9.5	8.3		La Jolla All	0.2415811	0.0000020	9.5	8.3	0.2364547	0.0000031	17.3	13.1	0.2364547	0.0000031	17.3	13.1		
0.5118026	0.0000008	-6.4	1.6	Ames 1-1	0.3484031	0.0000009	-5.9	2.6	0.72245	KREEP	0.2415805	0.0000011	7.0	4.6	0.72245	SAU 169-1-1	0.2415805	0.0000011	7.0	4.6	0.2364537	0.0000022	13.1	9.3	0.2364537	0.0000022	13.1	9.3		
0.5118026	0.0000008	-6.4	1.6	Ames 1-2	0.3484025	0.0000006	-7.6	1.7	0.72065	SAU 169-1-2	0.2415792	0.0000008	1.7	3.3	0.72065	SAU 169-1-2	0.2415792	0.0000008	1.7	3.3	0.2364515	0.0000017	3.8	7.2	0.2364515	0.0000017	3.8	7.2		
0.5117974	0.0000009	-6.6	1.8	Ames 1-3	0.3484006	0.0000006	-6.2	1.7	0.72087	SAU 169-2-3	0.2415780	0.0000008	-3.3	3.3	0.72087	SAU 169-2-3	0.2415780	0.0000008	-3.3	3.3	0.2364511	0.0000017	2.1	7.2	0.2364511	0.0000017	2.1	7.2		
0.5117974	0.0000009	-6.6	1.8	Ames 1-4	0.3483996	0.0000006																								

## REFERENCES

- Amelin Y. and Rotenberg E. (2004) Sm–Nd systematics of chondrites. *Earth Planet. Sci. Lett.* **223**, 267–282.
- Anders E. and Grevesse N. (1989) Abundances of the elements: Meteoritic and solar. *Geochim. Cosmochim. Acta* **53**, 197–214.
- Andreasen R. and Sharma M. (2006) Solar nebula heterogeneity in p-process samarium and neodymium isotopes. *Science* **214**, 806–809.
- Andreasen R. and Sharma M. (2009) Fractionation and mixing in a thermal ionization mass spectrometer source: implications and limitations for high-precision Nd isotope analyses. *Inter. J. Mass Spectrom.* **285**, 49–57.
- Andreasen R., Sharma M., Subbarao S. G. and Viladkar S. G. (2008) Where on Earth is the enriched Hadean reservoir? *Earth Planet. Sci. Lett.* **266**, 14–28.
- Arlandini C., Koppeler F., Wisshak K., Gallino R., Lugaro M., Busso M. and Straniero O. (1999) Neutron capture in low-mass asymptotic giant branch stars: cross sections and abundance signatures. *Astrophys. J.* **525**, 886–900.
- Beard B. L., Taylor L. A., Scherer E. E., Johnson C. M. and Snyder G. A. (1998) The source region and melting mineralogy of high-titanium and low-titanium lunar basalts deduced from Lu–Hf isotope data. *Geochim. Cosmochim. Acta* **62**, 525–544.
- Bennett V. C., Brandon A. D. and Nutman A. P. (2007) Coupled  $^{142}\text{Nd}$ – $^{143}\text{Nd}$  evidence for Hadean mantle dynamics. *Science* **318**, 1907–1910.
- Blichert-Toft J., Chauvel C. and Albarède F. (1997) Separation of Hf and Lu for high-precision isotope analysis of rock samples by magnetic sector-multiple collector ICP-MS. *Contrib. Mineral. Petrol.* **127**, 248–260.
- Borg L. E., Norman M., Nyquist L. E., Bogard D., Snyder G., Taylor L. and Lindstrom M. (1999) Isotopic studies of ferroan anorthosite 62236: a young lunar crustal rock from a light rare-earth-element-depleted source. *Geochim. Cosmochim. Acta* **63**, 2679–2691.
- Bourdon B., Touboul M., Caro G. and Kleine T. (2008) Early differentiation of the Earth and the Moon. *Phil. Trans. R. Soc. A.* [10.1098/rsta.2008.0125](https://doi.org/10.1098/rsta.2008.0125).
- Bouvier A., Blichert-Toft J., Moynier F., Vervoort J. D. and Albarède F. (2007) Pb–Pb dating constraints on the accretion and cooling history of chondrites. *Geochim. Cosmochim. Acta* **71**, 1583–1604.
- Bouvier A., Vervoort J. D. and Patchett J. P. (2008) The Lu–Hf and Sm–Nd isotopic composition of CHUR: constraints from unequilibrated chondrites and implications for the bulk composition of terrestrial planets. *Earth Planet. Sci. Lett.* **273**, 48–57.
- Boyet M. and Carlson R. W. (2005)  $^{142}\text{Nd}$  evidence for early (>4.53 Ga) global differentiation of the silicate Earth. *Science* **309**, 576–581.
- Boyet M. and Carlson R. W. (2007) A highly depleted Moon or a non-magma origin for the lunar crust? *Earth Planet. Sci. Lett.* **262**, 505–516.
- Brandon A. D., Norman M. D. and Debaille V. (2007) High-precision Nd isotopes in picrites from Hawaii and Iceland – no evidence for an early-formed enriched reservoir. *Eos Trans. AGU*, 88, Fall Meet. Suppl., Abstract V33A-1173.
- Caro G., Bourdon B., Birek J. L. and Moorbath S. (2003)  $^{146}\text{Sm}$ – $^{142}\text{Nd}$  evidence from Isua metamorphosed sediments for early differentiation. *Nature* **423**, 428–432.
- Caro G., Bourdon B., Wood B. J. and Corgne A. (2005) Trace-element fractionation in the Hadean mantle generated by melt segregation from a magma ocean. *Nature* **436**, 246–249.
- Caro G., Bourdon B., Birek J. L. and Moorbath S. (2006) High-precision  $^{142}\text{Nd}/^{143}\text{Nd}$  measurements in terrestrial rocks: constraints on the early differentiation of the Earth's mantle. *Geochim. Cosmochim. Acta* **70**, 164–191.
- Caro G., Bourdon B., Halliday A. N. and Quitte G. (2008) Superchondritic Sm/Nd in Mars, the Earth, and Moon. *Nature* **452**, 336–339.
- Carlson R. W. and Boyet M. (2008) Composition of the Earth's interior: the importance of early events. *Phil. Trans. R. Soc. A.* [10.1098/rsta.2008.0166](https://doi.org/10.1098/rsta.2008.0166).
- Carlson R. W., Boyet M. and Horan M. (2007) Chondritic barium, neodymium, and samarium isotope heterogeneity and early Earth differentiation. *Science* **316**, 1175–1178.
- Carlson R. W. and Lugmair G. W. (1979) Sm–Nd constraints on early differentiation and the evolution of KREEP. *Earth Planet. Sci. Lett.* **45**, 123–132.
- Chauvel C., Lewin E., Carpentier M., Arndt N. T. and Marini J. C. (2008) Role of recycled ocean basalt and sediment in generating the Hf–Nd mantle array. *Nat. Geosci.* **1**, 64–67.
- Debaille V., Brandon A. D., Yin Q. Z. and Jacobsen B. (2007) Coupled  $^{142}\text{Nd}$ – $^{143}\text{Nd}$  evidence for a protracted magma ocean in Mars. *Nature* **450**, 525–528.
- Debaille V., Yin Q. Z., Brandon A. D. and Jacobsen B. (2008) Martian mantle mineralogy investigated by the  $^{176}\text{Lu}$ – $^{176}\text{Hf}$  and  $^{147}\text{Sm}$ – $^{143}\text{Nd}$  systematics of shergottites. *Earth Planet. Sci. Lett.* **269**, 186–199.
- Debaille V., Brandon A.D., O'Neill C.O., Yin Q.Z., Jacobsen B. (2009). Isotopic evidence for mantle overturn in early Mars and its geodynamic consequences. *Nature Geosci.* doi: [10.1038/NNGEO579](https://doi.org/10.1038/NNGEO579).
- Elkins Tanton L. T., Van Orman J. A., Hager B. H. and Grove T. L. (2002) Re-examination of the lunar magma ocean cumulate overturn hypothesis: melting or mixing is required. *Earth Planet. Sci. Lett.* **196**, 239–249.
- Foley C. N., Wadhwa M., Borg L. E., Janney P. E., Hines R. and Grove T. L. (2005) The early differentiation history of Mars from 182W–142Nd isotope systematics in the SNC meteorites. *Geochim. Cosmochim. Acta* **69**, 4557–4571.
- Halliday A. N. (2000) Terrestrial accretion rates and the origin of the Moon. *Earth Planet. Sci. Lett.* **76**, 17–30.
- Halliday A. N. (2008) a young Moon-forming giant impact at 70–110 million years accompanied by late-stage mixing, core formation and degassing of Earth. *Phil. Trans. R. Soc. A.* [10.1098/rsta.2008.0209](https://doi.org/10.1098/rsta.2008.0209).
- Harper C. L., Nyquist L. E., Bansal B., Wiesman H. and Shih C. Y. (1995) Rapid accretion and early differentiation of Mars indicated by  $^{142}\text{Nd}/^{144}\text{Nd}$  in SNC meteorites. *Science* **267**, 213–217.
- Hart S. R. and Zindler A. (1989) Isotope fractionation laws: a test using calcium. *Int. Journal Mass Spectr. Ion Process.* **89**, 287–301.
- Hess P. C. and Parmentier E. M. (1995) A model for the thermal and chemical evolution of the Moon's interior: implications for the onset of mare volcanism. *Earth Planet. Sci. Lett.* **134**, 501–514.
- Humayun M. and Clayton R. N. (1995) Potassium isotope cosmochemistry: genetic implications of volatile element depletion. *Geochim. Cosmochim. Acta* **59**, 2131–2148.
- Jacobsen S. B. (1988) Isotopic and chemical constraints on mantle-crust evolution. *Geochim. Cosmochim. Acta* **52**, 1341–1350.
- Jacobsen S. B., Ranen M. C., Petaev M. I., Remo J. L., O'Connell J. O. and Sasselov D. D. (2008) Isotopes as clues to the origin and earliest differentiation history of the Earth. *Phil. Trans. R. Soc. A.* [10.1098/rsta.2008.0174](https://doi.org/10.1098/rsta.2008.0174).
- Lapen T. J., Mahlen N. J., Johnson C. M. and Beard B. L. (2004) High precision Lu and Hf isotope analyses of both spiked and unspiked samples. A new approach, *Geochem. Geophys. Geophys.* **5**, Q01010, [10.1029/2003GC000582](https://doi.org/10.1029/2003GC000582).

- Lingenfelter R. E., Canfield E. H. and Hampel V. E. (1972) The lunar neutron flux revisited. *Earth Planet. Sci. Lett.* **16**, 355–369.
- Ludwig K. R. (2003) IsoPlot version 3.0: a geochronological toolkit for Microsoft Excel. Berkeley Geochronology Center Special Pub 4, pp. 70.
- Lugmair G. W. and Galer J. G. (1992) Age and isotopic relationships among the angrites Lewis Cliff 86010 and Angra dos Reis. *Geochim. Cosmochim. Acta* **56**, 1673–1694.
- Lugmair G. W. and Marti K. (1971) Neutron capture effects in lunar gadolinium and the irradiation histories of some lunar rocks. *Earth Planet. Sci. Lett.* **13**, 32–42.
- Lugmair G. W. and Shukolyukov A. (1998) Early solar system timescales according to  $^{55}\text{Mn}$ – $^{53}\text{Cr}$  systematics. *Geochim. Cosmochim. Acta* **62**, 2863–2886.
- Meyer C. (2009) Lunar Sample Compendium. <http://curator.jsc.nasa.gov/lunar/compendium.cfm>.
- Münker C., Weyer S., Scherer E. E. and Mezger K. (2001) Separation of high field strength elements (Nb, Ta, Zr, Hf) and Lu from rock samples for MC-ICP-MS measurements. *Geochim. Geophys. Geosyst.* 2: Pap#2001GC000183.
- Nemchin A., Timms N., Pidgeon R., Geisler T., Reddy S. and Meyer C. (2009) Timing and crystallization of the lunar magma ocean constrained by the oldest zircon. *Nature Geosci.* **2**, 133–136.
- Norman M. D., Borg L. E., Nyquist L. E. and Borgard D. D. (2003) Chronology, geochemistry, and petrology of a ferroan noritic anorthosite clast from Descartes breccia 67215: Clues to the age, origin, structure, and impact history of the lunar crust. *Meteor. Planet. Sci.* **38**, 545–661.
- Nyquist L. E. and Shih C. Y. (1992) The isotopic record of lunar volcanism. *Geochim. Cosmochim. Acta* **56**, 2213–2234.
- Nyquist L. E., Bansal B., Wiesmann H. and Shih C. Y. (1994) Neodymium, strontium, and chromium isotopic studies of the LEW86010 and Angra dos Reis meteorites and the chronology of the angrite parent body. *Meteoritics* **29**, 872–885.
- Nyquist L. E., Wiesman H., Bansal B., Shih C. Y., Keith J. E. and Harper C. L. (1995)  $^{146}\text{Sm}$ – $^{142}\text{Nd}$  formation interval for the lunar mantle material. *Geochim. Cosmochim. Acta* **59**, 2817–2837.
- O’Neil J., Carlson R. W., Francis D. and Stevenson R. K. (2008) Neodymium-142 evidence for Hadean mafic crust. *Science* **321**, 1828–1831.
- O’Neill H. StC. and Palme H. (2008) Collisional erosion and the non-chondritic composition of the terrestrial planets. *Phil. Trans. R. Soc. A* **366**. doi:10.1098/rsta.2008.0111.
- Paces J. B., Nakai S., Neal C. R., Taylor L. A., Halliday A. N. and Lee D. -C. (1991) A strontium and neodymium isotopic study of Apollo 17 high-Ti mare basalts: Resolution of ages, evolution of magmas, and origins of source heterogeneities. *Geochim. Cosmochim. Acta* **55**, 2025–2043.
- Pahlevan K. and Stevenson D. J. (2007) Equilibration in the aftermath of the lunar-forming giant impact. *Earth Planet. Sci. Lett.* **262**, 438–449.
- Rankenburg K., Brandon A. D. and Neal C. R. (2006) Neodymium isotope evidence for a chondritic composition of the Moon. *Science* **312**, 1369–1372.
- Rankenburg K., Brandon A. D. and Norman M. D. (2007) A Rb–Sr and Sm–Nd isotope geochronology and trace element study of lunar meteorite LaPaz Icefield 02205. *Geochim. Cosmochim. Acta* **71**, 2120–2135.
- Rehkamper M., Gartner M., Galer S. J. G. and Goldstein S. L. (1996) Separation of Ce from other rare-earth elements with application to Sm–Nd and La–Ce chronometry. *Chem. Geol.* **129**, 201–208.
- Ringwood A. E. and Kesson (1976) A dynamic model for mare basalt petrogenesis. *Proc. Lunar Sci. Conf. 7th*, 1697–1722.
- Salters V. J. M. and Stracke A. (2004) Composition of the depleted mantle. *Geochem. Geophys. Geosyst.* **5**, Q05B07, 10.1029/2003GC000597.
- Sharma M. and Chen C. (2004) Neodymium isotope fractionation in the mass spectrometer and the issue of Nd-142 anomalies in early Archean rocks. *Precamb. Res.* **135**, 315–329.
- Shearer C. K. and Newsom H. E. (2000) W–Hf isotope abundances and the early origin and evolution of the Earth–Moon system. *Geochim. Cosmochim. Acta* **64**, 3599–3613.
- Snyder G. A., Taylor L. A. and Neal C. R. (1992) A chemical model for generating the sources of mare basalts: combined equilibrium and fractional crystallization of the lunar magma-shpere. *Geochim. Cosmochim. Acta* **56**, 3809–3823.
- Snyder G. A., Lee D. C., Taylor L. E., Halliday A. N. and Jerde E. A. (1994) Evolution of the upper mantle of the Earth’s Moon: Neodymium and strontium isotopic constraints from Hi–Ti mare basalts. *Geochim. Cosmochim. Acta* **58**, 4795–4808.
- Solomon S. C. and Longhi J. (1977) Magma oceanography: 1. Thermal evolution. *Proc. Lunar Planet. Sci. Conf. 8th*, 583–599.
- Spera F. (1992) Lunar magma ocean transport phenomena. *Geochim. Cosmochim. Acta* **56**, 2253–2265.
- Taylor D. J., McKeegan K. D. and Harrison T. M. (2009) Lu–Hf zircon evidence for rapid lunar differentiation. *Earth Planet. Sci. Lett.* **279**, 157–164.
- Tera F. and Wasserburg G. J. (1974) U–Th–Pb systematics on lunar rocks and inferences about lunar evolution and the age of the Moon. *Proc. Lunar Planet. Sci. Conf. 5th*, 1571–1599.
- Tonks W. B. and Melosh H. J. (1990) The physics of crystal settling and suspension in a turbulent magma ocean. In *Origin of the Earth* (eds N. E. Newsom and J. H. Jones). Oxford Univ. Press, New York., pp. 151–174.
- Touboul M., Kleine T., Bourdon B., Palme H. and Wieler R. (2007) Late formation and prolonged differentiation of the Moon inferred from W isotopes in lunar metals. *Nature* **450**, 1206–1209.
- Touboul M., Kleine T., Bourdon B., Palme H. and Wieler R. (2009) Tungsten isotope in ferroan anorthosites: implications for the age of the Moon and lifetime of its magma ocean. *Icarus* **199**, 245–249.
- Upadhyay D., Scherer E. E. and Mezger K. (2008) Fractionation and mixing of Nd isotopes during thermal ionization mass spectrometry: implications for high precision  $^{142}\text{Nd}/^{144}\text{Nd}$  analyses. *J. Anal. Atom. Spectrom.* **23**, 561–568.
- Upadhyay D., Scherer E. E. and Mezger K. (2009)  $^{142}\text{Nd}$  evidence for an enriched Hadean reservoir in cratonic roots. *Nature* **459**, 1118–1121.
- Unruh D. M., Stille P., Patchett P. J. and Tatsumoto M. (1984) Lu–Hf and Sm–Nd evolution in lunar mare basalts. *J. Geophys. Res.* **89**, B459–B477.
- Warren P. H. (2008) A depleted, not ideally chondritic bulk Earth: the explosive-volcanic basalt loss hypothesis. *Geochim. Cosmochim. Acta* **72**, 2217–2235.
- Wisshak K., Voss F., Kappeler F., Kazakov L. and Reffo G. (1998) Stellar neutron capture cross sections of the Nd isotopes. *Phys. Rev. C* **57**, 391–408.
- Wiechert U., Halliday A. N., Lee D. C., Snyder G. A., Taylor L. A. and Rumble D. (2001) Oxygen isotopes and the moon-forming giant impact. *Science* **294**, 345–348.
- Woolum D. S., Burnett D. S., Furst M. and Weiss J. R. (1975) Measurement of the lunar neutron density profile. *The Moon* **12**, 231–250.